iScience

CellPress
OPEN ACCESS

Review

Toward stable lead halide perovskite solar cells: A knob on the A/X sites components

Shurong Wang,[1] Aili Wang,[1] and Feng Hao[1,*]

SUMMARY

Hybrid lead halide ABX_3 perovskite solar cells (PSCs) have emerged as a strong competitor to the traditional solar cells with a certified power conversion efficiency beyond 25% and other remarkable features such as light weight, solution processability, and low manufacturing cost. Further development on the efficiency and stability brings forth increasing attention in the component regulation, such as partial or entire substitution of A/B/X sites by alternative elements with similar size. However, the relationships between composition, property, and performance are poorly understood. Here, the instability of PSCs from the photon-, moisture-, thermal-, and mechanical-induced degradation was first summarized and discussed. In addition, the component regulation from the A/X sites is highlighted from the aspects of band level alignment, charge-carrier dynamics, ion migration, crystallization behavior, residual strain, stoichiometry, and dimensionality control. Finally, the perspectives and future outlooks are highlighted to guide the rational design and practical application of PSCs.

INTRODUCTION

Organic-inorganic lead halide perovskite solar cells (PSCs) have emerged as one of the most attractive photovoltaic technology due to their impressive power conversion efficiency (PCE) accomplished over a short time. Their superior optoelectronic properties, such as long diffusion length up to 1 μm, small Urbach energy around 12.6 meV (Wang et al., 2016), low trap density of 10^{15}–10^{16} cm^{-3}(Baumann et al., 2015), high optical absorption coefficients about 10^5 cm^{-1}(Wang et al., 2015), small exciton binding energy (around 10–50 meV) (Grånäs et al., 2016; Quilettes et al., 2015), balanced ambipolar hole and electron transport and high charge carrier density (>10^{17} cm^{-2}) (Stranks et al., 2014), have attracted increasing attention for application in solar cells (Hao et al., 2014), photo-/radiation detectors (Venugopalan et al., 2019), light-emitting diodes (LEDs) (Zhang et al., 2020b), lasers (Wang et al., 2019d), and scintillators (Zhao et al., 2021; Zhu et al., 2020). In particular, the verified PCE of PSCs has swiftly climbed to a record of 25.5% (Min et al., 2021), on par with the high-efficiency silicon cells (Chen et al., 2020), cadmium telluride (CdTe), and copper-indium-gallium-arsenide (CIGS) cells. As for pure $FAPbI_3$ (FA^+ is formamidinium) perovskites, Hui et al. and Jeong et al. achieved a PCE of 24.10% and 25.21%, respectively (Table 1) (Hui et al., 2021; Jeong et al., 2021). Despite the $FAPbI_3$ devices achieving a high record PCE and long-term stability, the improved performance was achieved through appropriate additive engineering and solvent engineering beyond the scope of this review. It is comforting that the highest record of PCE appears on the mixed perovskite precursor with a structure of $FAPbI_3$:0.38$MDACl_2$ (where $MDACl_2$ is methylenediamine dihydrochloride) (Min et al., 2019, 2021). The characteristic diversity of perovskite structure and defect chemistry would lead to a further advance in photovoltaic devices and launch an appreciable revolution in the future photovoltaic market.

To form a stable ABX_3 structure, conventional A sites are monovalent cations such as methylammonium (MA^+), FA^+, and cesium (Cs^+), which occupied the octahedral cage composed of corner-shared $(BX_6)^{4-}$ octahedral. B sites are divalent metal ions (e.g., Pb^{2+} or Sn^{2+}) and generally have smaller ionic radius than A sites. X-site monovalent anions (e.g., Cl^-, Br^-, or I^-) usually coordinate with B sites to form the octahedral. In general, the optical and electronic properties of perovskites are closely related to their structure and composition. Empirically, the Goldschmidt's tolerance factor ($t=(r_A + r_X)/\sqrt{2}(r_B + r_X)$) of ABX_3 perovskite falls in the range of 0.825 ~1.059 to keep a high symmetrical cubic framework as well as high stability (Cheng and Lin, 2010; Travis et al., 2016). Moreover, Bartel et al. developed a more accurate tolerance factor (τ), which is defined as $T = r_A/r_B - n_A(n_A - r_A/r_B/\ln(r_A/r_B))$, where n_A is the oxidation state of A (Bartel

[1]School of Materials and Energy, University of Electronic Science and Technology of China, Chengdu 611731, China

*Correspondence: haofeng@uestc.edu.cn

https://doi.org/10.1016/j.isci.2021.103599

Table 1. Reported PCE and stability of PSCs with A/X sites engineering

Perovskites	Device structure	Test condition	Stability	PCE(%)	V_{oc} (V)	Year	Refs
Light stability							
$FA_{0.90}Cs_{0.10}PbI_3$	FTO/c-TiO_2//PVSK/Spiro-OMeTAD/Ag	under continuous white light (sulfur lamp, ≈100 mW cm^{-2}) illumination RH<50%, T < 65°C)	Retains over 70% of original PCE after 220 h at MPP	19.0	1.07	2015	Lee et al. (2015)
$Cs_{0.10}FA_{0.90}Pb(I_{0.83}Br_{0.17})_3$	FTO/c-TiO_2/Li-doped m-TiO_2/PVSK/Spiro-OMeTAD/Au	in N_2 atmosphere, held at 25°C under constant illumination	Remains over 90% of the original PCE over 250 h at MPP	21.17	1.15	2016	Saliba et al. (2016)
$(FAPbI_3)_{0.85}(MAPbBr_3)_{0.15}$	ITO/NiO_x/PVSK/$PC_{61}BM$/ZnO/Ag	RH 50% in dark at 25°C	Maintains over 80% of the original PCE for 3840 h	19.10	1.076	2018	Liu et al. (2018)
$FA_{0.83}Cs_{0.17}PbI_{2.7}Br_{0.3}$	FTO/SnO_2/$PC_{61}BM$/PVSK/PTAA/Au	under 10 sun illumination	Maintains over 90% of the original PCE for 150 h at MPP	22.5	1.214	2018	Wang et al. (2018b)
$FA_{0.75}Cs_{0..25}Pb(I_{0.80}Br_{0.20})_3$	ITO/PTAA/PVSK/C60/BCP/Ag	open-circuit voltage monitor at 0.1/1/10 sun	Retains over 100%, 98%, 88% after 10 min at 0.1, 1, 10 sun, respectively	17.4	1.17	2018	Bush et al. (2018)
$(FAPbI_3)_{0.95}(MAPbBr_3)_{0.05}$	FTO/c-TiO_2/m-TiO_2/PVSK/poly(3-hexylthiophene)/Au	under 1 sun illumination	Maintains over 95% of the original PCE for 1,370 h at MPP	23.3	1.152	2019	Jung et al. (2019)
(FA,MA,Cs)Pb(I,Br)$_3$(Cl)	FTO/SnO_2/PVSK:Eu^{3+}/Spiro-OMeTAD/Au	under 1 sun illumination	Maintains over 91% of the original PCE for 500 h at MPP	21.89	1.153	2019	Wang et al. (2019a)
$(FAPbI_3)_{0.92}(MAPbBr_3)_{0.08}$	ITO/SnO_2/PVSK/Spiro-OMeTAD/Ag	open-circuit condition exposed to continuous light (90 ± 10 mW cm^{-2}) under open-circuit condition exposed to continuous light (90 ± 10 mW cm^{-2}), RH 30–40%, 40°C, under open-circuit condition	Maintains over 95% of the original PCE for 720 h	23.48	1.191	2019	Wang et al. (2019b)
(Cs,FA,MA)Pb(I,Br)$_3$	ITO/NiO_x/F2HCNQ/PVSK/PCBM/BCP/Ag	encapsulated, RH 40% at 25°C	Maintains over 80% of the original PCE for >1000 h	22.13	1.14	2020	Ru et al. (2020)
$(MTEA)_2(MA)_4Pb_5I_{16}$	ITO/PEDOT:PSS/PVSK/$PC_{61}BM$/BCP/Cr/Au	under simulated AM1.5G light (Enlitech SS-F5-3A) in N_2 atmosphere	Retains 85% of the original PCE after 1000 h at MPP	18.06	1.09	2020	Ren et al. (2020)
$BA_2MA_3Pb_4I_{13}$	ITO/SnO_2/PVSK/Spiro-OMeTAD/Au	under continuous 1 sun, AM1.5G illumination	Retains 90% of the original PCE after 1100 h	16.25	1.31	2020	Liang et al. (2021)
$GA_{0.015}Cs_{0.046}MA_{0.152}FA_{0.787}Pb(I_{0.815}Br_{0.185})_3$	FTO/c-TiO_2/Li-doped m-TiO_2/PVSK/Spiro-OMeTAD/Au	under illumination (AM1.5G 100 mW cm^{-2})	Retains over 90% of the original PCE after 3000s at MPP	20.16	1.18	2020	Jung et al. (2020)
$Cs_{0.5}FA_{0.5}PbI_3$ QDs	ITO/SnO_2/PVSK/Spiro-OMeTAD/Au	at open circuit under 1 sun illumination in N_2 at 50–65°C	Retains over 94% of the original PCE for 600 h	16.6	1.17	2020	Hao et al. (2020)

(*Continued on next page*)

Table 1. *Continued*

Perovskites	Device structure	Test condition	Stability	PCE(%)	V_{oc} (V)	Year	Refs
$(Cs,FA,MA)Pb(I,Br)_3$	ITO/PTAA/PVSK/C60/BCP/Cu	under 1 sun in N_2 atmosphere with a UV filter with a 420-nm cut-off	Maintains over 99% of the original PCE for 1000 h at MPP	23.0	1.17	2020	Zheng et al. (2020)
$FA_{0.92}Cs_{0.08}PbI_3$	ITO/PTAA/PVSK/C60/BCP/Cu	at 50 ± 5°C in air under 1 sun illumination.	Maintains 93.6% of the original PCE for over 1000 h	20.2	–	2021	Deng et al. (2021)
$Cs_{0.04}(FA_{0.84}MA_{0.16})_{0.96}Pb(I_{0.84}Br_{0.16})_3$	ITO/SnO_2/PVSK/Spiro-OMeTAD/Au	under continuous 1 sun illumination in N_2 atmosphere at 40°C	Retains over 82% of the original PCE after 1000 h at MPP	22.2	1.18	2021	Dong et al. (2021)
$FA_{1-x}MA_xPbI_3$	ITO/SnO_2:$CoCl_2$/PVSK/Spiro-OMeTAD/Au	under continuous irradiation	Retains 83.5% of the original PVE after 200 h	23.82	1.20	2021	Wang et al. (2021b)
$FA_{1-x}MA_xPbI_yBr_{3-y}$ (Cl)	FTO/c-TiO_2/Li-doped m-TiO_2/PVSK/Spiro-OMeTAD/Au	LED source, 1 sun in N_2 atmosphere at 25°C	Remains 90% of the original PCE after 400 h	22.30	1.15	2021	Alharbi et al. (2021)
Moisture stability							
$FA_{0.85}MA_{0.15}Pb(I_{0.85}Br_{0.15})_3$	ITO/PTAA/PVSK/C60/BCP/Cu	RH 50–85% in N_2 atmosphere at 25°C	Retains almost 100% of the original PCE over 720 h	21.0	1.14	2017	Zheng et al. (2017)
$(FAPbI_3)_{0.95}(MAPbBr_3)_{0.05}$	FTO/c-TiO_2/m-TiO_2/PVSK/Poly(3-hexylthiophene)/Au	under 85% relative humidity at room temperature	Maintains nearly 80% of its initial PCE after 1,008 h	23.3	1.152	2019	Jung et al. (2019)
$(Cs,FA,MA)Pb(I,Br)_3$	ITO/PTAA/PVSK/C60/BCP/Ag	RH 60–65%, at room temperature	Maintains nearly 90% of its initial PCE after 1700 h	21.0	1.12	2020	Hu et al. (2020)
$Cs_{0.05}(FA_{0.83}MA_{0.17})_{0.95}Pb(I_{0.83}Br_{0.17})_3$	FTO/c-TiO_2/m-TiO_2/PVSK/Spiro-OMeTAD/Au	under ambient condition in a dry room with an aluminum foil (RH: 20%–35%)	Retains over 95% of the original PCE over 3024 h	20.8	1.14	2018	Singh and Miyasaka (2018)
$(FAPbI_3)_{0.9}(MAPbBr_3)_{0.1}$	–	single crystal, in a desiccator with an RH 20% and characterized at intervals during 10,000 h aging time more than a year)	at least a 10,000 h water-oxygen stability	–	–	2019	Chen et al., 2019b
$Gua_y(FAMA)_{1-y}PbI_xCl_{3-x}$	ITO/SnO_2/PVSK/Spiro-OMeTAD/Ag	RH 25% at 25°C	Retains 80% of the original PCE over 800 h	21.3	1.14	2021	Wang et al. (2021c)
$(MTEA)_2(MA)_4Pb_5I_{16}$	ITO/PEDOT:PSS/PVSK/PC_{61}BM/BCP/Cr/Au	RH 80% (±7%) at 25°C	Retains 70% of the original PCE over 1512 h	18.06	1.09	2020	Ren et al. (2020)
$BA_2MA_3Pb_4I_{13}$	ITO/SnO_2/PVSK/Spiro-OMeTAD/Au	RH 65 ± 10%	Retains over 90% of the original PCE after 4680 h	16.25	1.31	2020	Liang et al. (2021)
$(FAPbI_3)_{0.85}(MAPbBr_3)_{0.15}$	FTO/c-TiO_2/m-TiO_2/PVSK/Spiro-OMeTAD/Au	RH 75%	Retains over 87% of the original PCE after 912 h	21.7	1.17	2018	Cho et al. (2018)
$FAPbI_3$ with $MDACl_2$	FTO/c-TiO_2/m-TiO_2/PVSK/Spiro-OMeTAD/Au	RH 85% at 25°C	Retains over 90% of the original PCE after 70 h	24.66	1.14	2019	Min et al. (2019)
$FA_{1-x}MA_xPbI_3$	FTO/c-TiO_2/m-TiO_2/PVSK/Spiro-OMeTAD/Au	unencapsulated in ambient conditions with RH. 50%	Retains over 90% of the original PCE after 2200 h	22.02	1.108	2021	Yang et al. (2021)
$FAMAPbI_{3-x}Cl_x$	FTO/NiO_x/PVSK/PC_{61}BM/BCP/Ag	in ambient air with RH ≤ 30%	Retains over 96% of the original PCE after 1020 h.	20.2	1.12	2018	Liu et al. (2018)
(FA,MA,Cs)$Pb(I,Br)_3$(Cl)	FTO/SnO_2/PVSK:Eu^{3+}/Spiro-OMeTAD/Au	in N_2 atmosphere	Retains over 90% of the original PCE after 8000 h	21.89	1.153	2019	Wang et al. (2019a)

(*Continued on next page*)

Table 1. *Continued*

Perovskites	Device structure	Test condition	Stability	PCE(%)	V_{oc} (V)	Year	Refs
$(CsPbI_3)_{0.05}[(FAPbI_3)_{0.90}(MAPbBr_3)_{0.10}]_{0.95}$	ITO/PTAA/PVSK/PC_{61}BM/Cl/Ag(Au)	in N_2 atmosphere	Retains over 99% of the original PCE after 4080 h	21.29	1.07	2021	Wang et al. (2021a)
Thermal stability							
$BA_2(MA_{0.76}FA_{0.19}Cs_{0.05})_3Pb_4I_{13}$	ITO/MoO_3/PEDOT:PSS/RP PVSK/PC_{61}BM/BCP/Ag	at a constant temperature of 85°C in the dark	Retains 80% of the original PCE after over 1400 h	15.58	1.08	2019	Jiang et al. (2019)
$MA_{1-x}ClEA_xPbI_3$	FTO/c-TiO_2/m-TiO_2/PVSK/Spiro-OMeTAD/Au	variable temperatures under MPP tracking and ~0.7 sun illumination	Retains over 86% after 250 h	18.28	1.07	2019	Shirzadi et al. (2019)
$MA_{0.6}FA_{0.4}PbI_{2.8}Br_{0.2}$	ITO/PEDOT:PSS/PVSK/C60/BCP/Ag	100 mW cm^{-2}, AM 1.5G) with thermal cycling between 25 and 85°C according to the ISOS-T-1 standard under open-circuit condition	Slightly reduced after burn-in period over 800 h	14.83	1.01	2019	Qin et al. (2019a)
$BA_2MA_3Pb_4I_{13}$	ITO/SnO_2/PVSK/Spiro-oMeTAD/Au	under operation at 85°C	Retains 90% of the original PCE after 558 h	16.25	1.31	2020	Liang et al. (2021)
$FAPbI_3$ with $MDACl_2$	FTO/c-TiO_2/m-TiO_2/PVSK/Spiro-OMeTAD/Au	at 150°C and ~25% RH	Retains over 90% of the original PCE after 17 h	24.66	1.14	2019	Min et al. (2019)
$Cs_{0.99}Rb_{0.01}PbI_2Br$	FTO/c-TiO_2/m-TiO_2/PVSK/Spiro-OMeTAD/Au	RH 40% at 65°C without encapsulation	Retains over 90% of the original PCE after 120 h	17.16	1.32	2020	Patil et al. (2020)
$Rb_{0.05}Cs_{0.05}FA_{0.75}MA_{0.15}Pb(I_{0.83}Br_{0.17})_3$	FTO/c-TiO_2/m-TiO_2/PVSK/PTAA/Au	at 85°C/85% RH under AM 1.5G irradiation (100 mW cm^{-2})	Retains over 92% of the original PCE after 1000 h	20.1	1.103	2019	Matsui et al. (2019)
$FA_{1-x}MA_xPbI_3$	ITO/SnO_2/PVSK/PEAI/Spiro-OMeTAD/Au	85°C at N_2 glove box	Retains over 80% of the original PCE after 500 h	23.56	1.16	2019	Wang et al. (2021b)
(FA,MA,Cs)Pb(I,Br)$_3$(Cl)	FTO/SnO_2/PVSK:Eu^{3+}/Spiro-OMeTAD/Au	85°C	Retains over 91% of the original PCE after 1000 h	21.89	1.153	2019	Wang et al. (2019a)
$(Cs_{0.15}FA_{0.85})Pb(I_{0.9}Br_{0.1})_3$	FTO/NiO_x/Zn:$CuGaO_2$/PVSK/PCBM/BCP/Ag	85°C in N_2 atmosphere	Retains over 85% of the original PCE after 1000 h	20.67	1.112	2019	Chen et al. (2019b)
(Cs,FA,MA)Pb(I,Br)$_3$	ITO/PTAA/PVSK/C60/BCP/Ag	85°C in N_2 atmosphere	Retains over 95% of its original PCE after 1000 h	21.0	1.12	2020	Hu et al. (2020)
Mechanical stability							
$Cs_{0.04}(FA_{0.84}MA_{0.16})_{0.96}Pb(I_{0.84}Br_{0.16})_3$	ITO/SnO_2/PVSK/Spiro-OMeTAD/Au	mechanical bending cycles (40% RH; ambient air; 25°C; 3mm minimum r)	Retains 85% of the original PCE after 2500 bending cycles	20.1	1.15	2021	Dong et al. (2021)
$Cs_{0.05}(FA_{0.92}MA_{0.08})_{0.95}Pb(I_{0.92}Br_{0.08})_3$	ITO/PTAA/PVSK/PM6:CH1007:PCBM/$Zr(acac)_4$/Ag	under continuous illumination	Retains 95% of the original PCE after 1000 bending cycles	21.73	1.13	2021	Wu et al. (2021)
PCE and stability in pure perovskites							
$MAPbI_3$	ITO/NiO_x/PVSK/PCBM/BCP/Ag	–	–	22.32	1.16	2021	Wang et al., 2020a
$FAPbI_3$	FTO/c-TiO_2/m-TiO_2/PVSK/Spiro-*m*F/Au	50% RH in the air without encapsulation	Retains 87% of the original PCE after 500 h	24.50	1.16	2020	Jeong et al. (2020)

(*Continued on next page*)

Table 1. *Continued*

Perovskites	Device structure	Test condition	Stability	PCE(%)	V_{oc} (V)	Year	Refs
$FAPbI_3$	FTO/c-TiO_2/m-TiO_2/PVSK/Spiro-OMeTAD/Au	60°C under 20% RH	Retains 80% of the original PCE after 1000 h	25.21	1.17	2021	Jeong et al. (2021)
$FAPbI_3$	ITO/SnO_2/PVSK/Spiro-OMeTAD/MoO_3/Au	85°C in N_2 atmosphere	Retains 80% of the original PCE after 500 h	24.10	1.17	2021	Hui et al. (2021)

$MDACl_2$: methylenediammonium dichloride, PEAI: 2-phenylethanamine iodide, F2HCNQ: 3,6-difluoro-2,5,7,7,8,8-hexacyanoquinodimethane, IP: piperazinium iodide, CI: cathode interlayer, BA: $CH_3(CH_2)_3NH_3$, FI–SnO_2: FAI-incorporated SnO_2, MTEACl: 2-(methylthio)ethylamine hydrochloride, PM6: poly[(2,6-(4,8-bis(5-(2-ethylhexyl-3-fluoro)thiophen-2-yl)-benzo[1,2-b:4,5-b′]dithiophene))-alt-(5,5-(1′,3′,di-2-thienyl-5′,7′-bis(2-ethylhexyl) benzo[1′2′-c:4′5′-c′]dithiophene-4,8-di-one)], CH1007:2,10-bis (2-methylene-(3-(1,1-dicyano- methylene)-5,6-difluoroindanone))-12,13-bis(2-butyl-octyl)-3,9-diundecyldiselenopheno[2″,3′′:4′5′]thieno[2′,3′:4,5]pyrrolo[3,2-e:2′,3′-g][2,1,3]benzothiadiazole.

et al., 2019). Massive attempts on composition engineering have been explored to modulate the physical/chemical properties of perovskites. Notably, the complicated features of spatial framework in A/B/X sites also affect the PCE and stability of corresponding PSCs. Several theoretical design methodologies (Saliba, 2019), such as high-throughput screening, machine learning, and data mining, also have been explored to drive the elemental substitutions and multidimensional researches.

Perovskite precursors have low formation enthalpy and hygroscopic characteristics, which makes the crystallization and morphology highly important to obtain uniform and pinhole-free thin films. For both n-i-p and inverted p-i-n PSC devices, optimizing the compositions would further approach the theoretical Shockley-Queisser (S-Q) efficiency limit (the S-Q limit for $APbX_3$ is limited to 32% since its band gap is >1.5 eV) (Shockley and Queisser, 1961). Historically, the organic cations on A sites evolved from MA^+ to FA^+/MA^+, and further to $Cs^+/FA^+/MA^+$ for high-performance devices. Simultaneously, the anions on X sites changed with the sequence of I^- to I^-/Cl^-, and further to I^-/Br^-. Although more types of mixed X site (such as Br^-/Cl^-) in published literature (Sedighi et al., 2016), here we focused on the mixed X-site type ($APbI_yBr_{1-y}$) in the following discussion. Those approaches declare the crucial role of components regulation in boosting the efficiency and operational stability under external stimuli stress (e.g., light, moisture, thermal, and mechanical). The Pb^{2+} in B site can be replaced with cations with similar outer shell electron configurations, such as Sn^{2+} and Ge^{2+} in the IVA group with ABX_3 structure, or heterovalent cations such as Sb^{3+} and Bi^{3+} in the VA group and Ag^+, Cu^+, and Au^+ to yield a double perovskite lattice with a general formula of $A_2B^+B^{3+}X_6$ (Cortecchia et al., 2016; Jin et al., 2020b; Krishnamoorthy et al., 2015; Slavney et al., 2016; Wang et al., 2021d). However, the Sn PSCs still showed poor performance and stability due to the adverse oxidation from Sn^{2+} to Sn^{4+} and fast crystallization. When discussing the Ge-based PSCs, the $4s^2$ electronic configuration of Ge^{2+} could easily lose their lone pair electrons and lead to poor stability (Stoumpos et al., 2015). Despite the stable characteristic of double perovskites in ambient conditions, they have relatively poor photovoltaic performance influenced by other factors, such as strong localized resonant excitons, giant electron-phonon coupling, intermediate electron masses, and high density of electron traps (Biega et al., 2021; Longo et al., 2020; Steele et al., 2018; Volonakis et al., 2016). The trivalent Sb^{3+} and Bi^{3+} can easily form layer vacant structures when only considering one metal cation, which further limits the charge transport of these materials(Jin et al., 2020b).

Therefore, our review focused on the A/X sites in Pb-based PSCs. Their intrinsic instability of halide perovskite films should be identified. The feasibility of component engineering from the A/X sites is underscored in this review. We focus on the structural properties and photoelectric characteristics to discuss the relationships between efficiency and stability. The component alloying would offer a powerful direction for understanding how detailed changes at A/X sites drive the structural and photovoltaic properties, which in turn act as a comprehensive knob to guide the semiconductor characteristic.

THE INSTABILITY OF PSCS

Generally, illumination, moisture, elevated temperature, and mechanical force all cause non-negligible degradation of perovskite materials and further turn into instability in PSC devices (Hong et al., 2019; Soon et al., 2013). We explored how external factors affect the propensity of ABX_3 perovskites toward instability on pure and mixed perovskites.

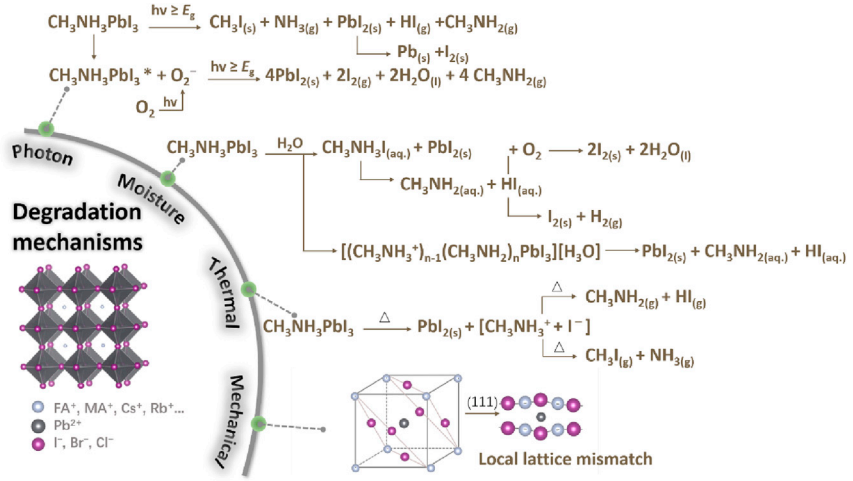

Figure 1. The instability of perovskites under photon/moisture/thermal/mechanical stress.

Photon-induced degradation

Photon-induced degradation in pure perovskites

The $MAPbI_3$ perovskites could induce the formation of PbI_2 under white illumination, following spreading over the whole crystal (Zu et al., 2017). Meanwhile, the N and C escape from $MAPbI_3$ lattice in the form of NH_3, MA gas, and exited CH_3I, respectively (details see Figure 1). The PbI_2 further decomposes to the metallic Pb. Since 2016, Haque et al. have demonstrated that the formation of superoxide (O_2^-) can deprotonate MA^+ of photo-excited MA*, further leading to the formation of PbI_2, H_2O, MA, and I_2 as shown in Figure 2A (Akbulatov et al., 2017; Aristidou et al., 2017). Moreover, the O_2-catalyzed degradation inevitably reduces the yield of a photo-induced carrier to a large extent. Interestingly, the O_2^- can occupy the I^- vacancies due to similar size between O_2^- and I^- (Figure 2B), thus restoring the octahedral coordination of Pb^{2+}. The characteristic photo-oxidative degradation mechanism of $MAPbI_3$ (001) surface was revealed further (Ouyang et al., 2019). It mainly contains three key steps (Figure 2C): the generation of O_2^- on the surface under illumination, rapid oxidation and yield of H_2O and $Pb(OH)_2$ on the surface perovskites, and then slow hydration of inner perovskites. O_2 plays a key role in photo-induced instability via Brønsted–Lowry acid-base reaction between O_2^- and MA^+(Nickel et al., 2017). Therefore, the existence of O_2 accelerates the degradation process of halide perovskite films.

Besides, photons with high energy would break the N-H bonding and accumulate the cation vacancies at the electrode, resulting in reversible degradation under operation. Mohite et al. investigated the light-activated photocurrent degradation mechanisms of PSCs, which was ascribed to the effect of photochemical and field-assisted ion migration (Bi et al., 2017). More importantly, the light-activated meta-stable trap states trigger increased nonradiative recombination, following the involved ion migration, ferroelectricity, intrinsic defects, and enhanced photo-generation of polaronic states (Hoke et al., 2015; Xiao et al., 2015). Conversely, the self-healing behavior also happens by resting the device a few minutes under dark conditions, which contribute to the longer timescales migration of cation vacancies (around 10^3 s) than halide vacancies (Domanski et al., 2017; Wei et al., 2020). Abate et al. proved the mobility and distribution of cation and halide vacancies, where the cation and anion vacancies are randomly distributed in the lattice initially, and then halide vacancies migrate and form a Debye layer accompanied by immobile cation vacancies behind up to 10^2 s under illumination, and finally, cation vacancies form an additional Debye layer and inhibit charge extraction (Figure 2D).

Photon-induced degradation in mixed perovskites

As for mixed halide perovskites, the phase segregation can be seduced easily under illumination, leading to optical instability. This phenomenon is called the Hoke effect (Brennan et al., 2020; Hoke et al., 2015). McGehee et al. found that the $MAPb(Br_xI_{1-x})_3$ perovskites segregated into two phases containing the Br^--rich majority and I^--rich minority under light soaking (Hoke et al., 2015). The I^--rich domains stabilize the holes and provide a driving enthalpy for photoinduced phase segregation. By selective injection of

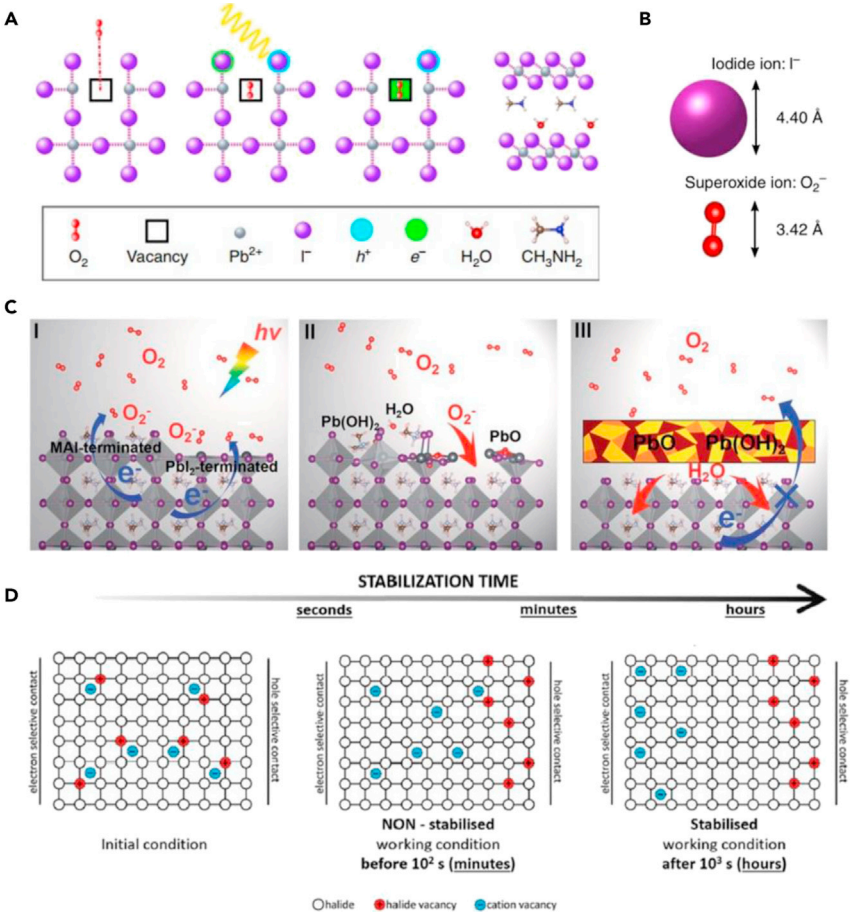

Figure 2. Photon-induced degradation mechanism of perovskites

(A) Schematic patterns of the reaction steps of O_2 with $MAPbI_3$.

(B) Comparison of the relative size of I^- and O_2^-. Credit adapted from (Aristidou et al., 2017).

(C) Schematic patterns of the photo-oxidative degradation process of $MAPbI_3$ perovskites along (001) plane. Credit adapted from (Ouyang et al., 2019).

(D) Schematic patterns of ion distribution within the perovskite layer under working conditions from initial, non-stabilized state of minutes, and stabilized state on the timescale of hours. Credit adapted from (Domanski et al., 2017).

holes in $MAPbBr_{1.5}I_{1.5}$ perovskites, Janaky et al. revealed that the I^- expelled and left behind re-formed $MAPbBr_3$ domains (Samu et al., 2019). The weakening of Pb-I bonding due to the hole trapping (oxidation of I sites) and the expulsion from the lattice (excited as I site) further results in severe phase segregation. Therefore, the key factor toward improving the operational stability of PSCs is to balance the chemical equilibrium between the photon-induced decomposition processes and self-healing reactions. To improve the photon-induced stability, mixed perovskite by 5% Cs^+ partially replacing MA^+ with a structure of $MA_{0.95}Cs_{0.05}PbI_3$ could simultaneously suppress the formation of O_2^- and ion migration of I vacancies via enhancing the energy barrier of ions (Lin et al., 2021). Indeed, lattice symmetry in mixed perovskite under photo illumination is reliable and, therefore, in favor of improved charge carrier recombination properties (Kim and Hagfeldt, 2019). Perovskite components indicated superb performance in stable 3D perovskite structure and increased photon-induced stability by A/X sites synergy effects.

Moisture-induced degradation

Moisture-induced degradation in pure perovskites

Undoubtedly, the moisture-induced degradation of PSCs is an intractable issue before commercialization. Water, like a Lewis base, could coordinate with $MAPbI_3$ and form $([MA^+]_{n-1}[MA]_nPbI_3)(H_3O)$ intermediate, then further decompose to HI, MA, and PbI_2 in the end (Figure 1). (Frost et al., 2014) Interestingly, the

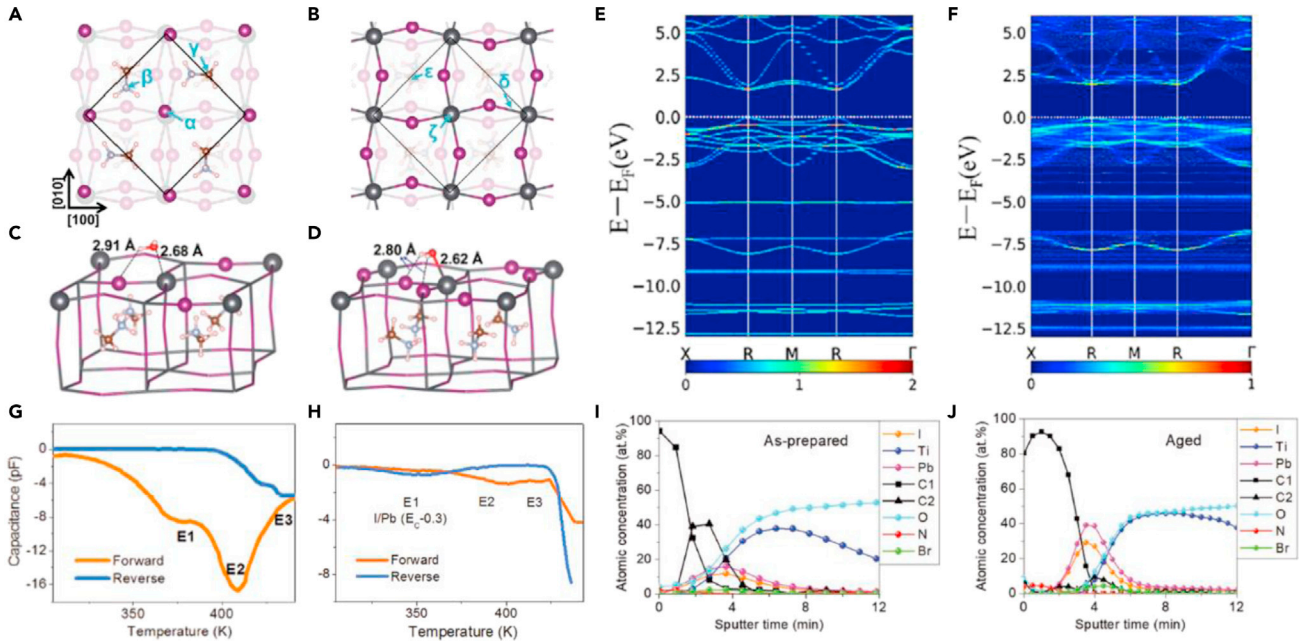

Figure 3. Moisture-induced degradation mechanism of perovskites

Water adsorption sites on $MAPbI_3$ (001) surface in (A) top-down view of the MAI-termination and (B) side-down view of the MAI-terminated P^+ surface. Water adsorption to (C) the PbI_2-terminated P^+ surface and (D) PbI_2-terminated P^- surface. Credit adapted from (Koocher et al., 2015). The band structures of (E) $MAPbI_3$ and (F) $MAPbI_3$ with four-absorbed H_2O molecules in on supercell. Credit adapted from (He et al., 2018). Deep-level transient spectroscopy (DLTS) spectra with different various bias voltage for the deep-level defects of (G) fresh and (H) aged $(FAPbI_3)_{0.85}(MAPbBr_3)_{0.15}$. Auger electron spectroscopy (AES) depth profiles of the (I) fresh and (J) aged $(FAPbI_3)_{0.85}(MAPbBr_3)_{0.15}$. Credit adapted from (Heo et al., 2019).

presence of liquid H_2O could form irreversible decomposition when exposed to high humidity, in contrast to H_2O in the vapor state (Leguy et al., 2015b). While the irreversible decomposition of $MAPbI_3$ exposing in H_2O vapor occurred once the grain converted to monohydrate phase ($MAPbI_3{\cdot}H_2O$).

Another moisture-induced degradation is accompanied by the formation of MAI, MA, and HI (Niu et al., 2015). On the one hand, the HI could decompose into H_2 and I_2 via photochemical reaction under UV illumination. On the other hand, the presence of HI drives the formation of I_2 and H_2O via redox reaction in an O_2 atmosphere (Figure 1). Barnes et al. demonstrated that the hydration process caused irreversible efficiency loss due to grain isolation by hydrated crystal, which impedes the charge carrier transport and results in nonradiative recombination at the grain interface (Leguy et al., 2015b; Zhang et al., 2020a). Rappe et al. investigated the interaction and polarization effect between (001) surface of $MAPbI_3$ perovskite and H_2O by density functional theory (DFT) as shown in Figures 3A–3D (Koocher et al., 2015). For the MA-terminated surface (Figures 3A and 3B), it showed higher water resistance in CH_3-end pointing than in NH_3^+-ends pointing because of small water reactivity. Moreover, the intensity of water adsorbate configuration on the PbI_2-terminated surface (Figures 3C and 3D) in NH_3^+-end pointing is the lowest, where the location of H_2O is almost planar in (001) surface. The stronger Pb-O bonding is formed on the PbI_2-terminated surface in CH_3-end pointing due to the weakened splitting of Pb *p* orbital. The degradation mechanism depends on the formation of hydrogen bonds between the surface MA^+ cations and H_2O, leading to large adsorption energy (Zhang and Sit, 2015). Therefore, exploiting applicable strategies by inducing an electric field and dipoles with local or interfacial order as a shielding layer is conducive for enhanced moisture stability.

Besides, the I^- vacancy, the most common point defect in $MAPbI_3$ perovskite could facilitate the migration and reduced diffusion barrier of H_2O (He et al., 2018). The near-gap electronic states show significant changes after introducing H_2O in the lattice, resulting in an increased band gap (from 1.55 eV to 1.84 eV) accordingly (Figures 3E and 3F). Indeed, when the decomposition occurs, the mobile I^- diffuses from absorption layer to electrode, which unveils the device degradation process under environmental stimulations.

Moisture-induced degradation in mixed perovskites

Different from $MAPbI_3$ perovskites, there are three main defects in $(FAPbI_3)_{0.85}(MAPbBr_3)_{0.15}$ perovskites: I_{Pb} (I atoms occupying at Pb sites), I_{MA} (I atoms occupying at MA sites), and Pb_{Br} (Pb atoms occupying at Br sites). Nazeeruddin et al. indicated that MA would evaporate off following the formation of PbI_2 with a widened band gap (Heo et al., 2019). The defect states of E2 and E3 (assigned to I_{MA} and Pb_{Br} defects) in Figures 3G and 3H remained, while E1 (assigned to I_{Pb} defect) disappeared after aged about 6 months. The change of composition in Figures 3I and 3J implied that the ratio of I/Pb remained unchanged, while the ratio of C/Pb was decreased after a long-time age in the air. In PSCs, the Fermi level (E_f) could be held at the defect states due to the presence of deep-level defects, which is deemed to be a key factor for high V_{oc} (Heo et al., 2017). Since the E_f of mixed perovskite depends on the I_{MA} defect (deep-level defects), reducing the loss of MA molecule is a key to fulfilling device stability. Park et al. have proved that 10% Cs^+ substitution in $FAPbI_3$ perovskites could enhance the interaction between I^- and FA^+ due to contraction of cubo-octahedral volume, which significantly improved the moisture stability along with photovoltaic performance (Lee et al., 2015). The 5% Cs^+ incorporation in mixed $(FA_{0.83}MA_{0.17})Pb(I_{0.83}Br_{0.17})_3$ perovskites stabilized the perovskite phase when exposed to a humid atmosphere. Therefore, the cations and halides synergistically affect the structural stability. Combining Cs^+ and Br^- are indeed necessary to achieve superior stable mixed perovskite alloys. Chen et al. have proved that bond length of Pb-I was elongated in $(FAPbI_3)_{0.9}(MAPbBr_3)_{0.05}(CsPbBr_3)_{0.05}$ perovskites, compared with $(FAPbI_3)_{0.9}(MAPbBr_3)_{0.1}$ perovskites, which further enhanced interaction between the cation and inorganic octahedral framework and reduced the formation of I^- vacancies (Chen et al., 2019a).

Thermal-induced degradation

Similarly, PSC devices are also subjected to thermal degradation when the ambient temperature is over 45°C or even higher. The resultant phenomenon such as ion migration and phase transition/separation could block charge transport. Based on the international test standard, thermal stability at 85°C is required according to IEC 61646 climatic chamber tests. Generally, single A-site perovskites have imperfections in-phase/thermal instability. Mixed perovskites have been confirmed with improved optoelectronic properties and thermal stability. A-site cations (such as FA^+ and MA^+) could not contribute to the electronic states near band edges, whereas the A-site trap defects could affect the defect formation energies of $(PbX_6)^{4-}$ octahedral framework (Fang et al., 2021). Therefore, the A sites alloys have a great influence on thermal stability through altering lattice parameters (e.g., lattice contraction or dilation of Pb-X lattice) and octahedral tilting (Amat et al., 2014) Similar to the moisture-induced degradation, the observed thermal degradation root in the formal loss of MAX, as well as halogen substitution reaction and reduction reaction from Pb^{2+} to metallic Pb^0 (Akbulatov et al., 2017).

Noteworthy, the $FAPbI_3$ perovskite undergoes cubic-to-hexagonal transition at room temperature with large thermal hysteresis and intrinsic instability. The organic cations play a key role in structural stability through the entropy contribution in Gibbs free energy (Chen et al., 2016). The FA^+ cation in the cubic phase ($Pm\bar{3}m$ symmetry) of $FAPbI_3$ perovskite has large entropy with isotropic orientation to stabilize the cubic phase upon 350 K. When cooling at 290 K, the FA^+ cation in hexagonal phase ($P6_3/mmc$ symmetry) has low entropy with strong preferential orientations. Qi et al. used two assessment parameters (T_d, degradation temperature, and Q_{HAMDR}, lower maximum degradation rate) to reflect the thermodynamic stability, where the low T_d and Q_{HAMDR} imply low kinetic thermal stability for perovskites (Figures 4A–4C) (García-Fernández et al., 2018). The order of Q_{HAMDR} criterion is α-$FAPbI_3$<α-$FAPbBr_3 \approx$ $MAPbI_3$< $MAPbBr_3$< $MAPbCl_3$, respectively (Nagabhushana et al., 2016). Accurately, incorporating inorganic Cs^+ in mixed perovskites can capture thermal stability via Q_{HAMDR} improvement. The trend of degradation energy (E_d) and cohesive energy (E_c) should locate at $E_d \geq$ 130 kJ mol^{-1} and $E_c \geq$ 4500 kJ mol^{-1} to ensure minimal decomposition.

Further, Qi et al. proposed another thermal degradation mechanism and verified it by hypothetical thermodynamic cycle, where the major decomposition product is CH_3I and NH_3 (Figure 4D) (Juarez-Perez et al., 2016) The pre-formed NH_3 can react with MA^+ via acid-base reaction and finally form the tertiary amine $(CH_3)_3N$ in PbI_3^- octahedral network. However, this reaction is negligible in the bulk perovskites due to the trapping barrier of MA^+ ions, which can explain the rarely observed $(CH_3)_3N$ during the thermal degradation process. It is reasonable that the thermal decomposition in mixed perovskites is much slower than pure $MAPbI_3$ perovskites. Different from the water-catalyzed progress of MA^+/FA^+ ions in perovskite compositions, MA^+ cations involve the first stage of thermal degradation and the second process turns to

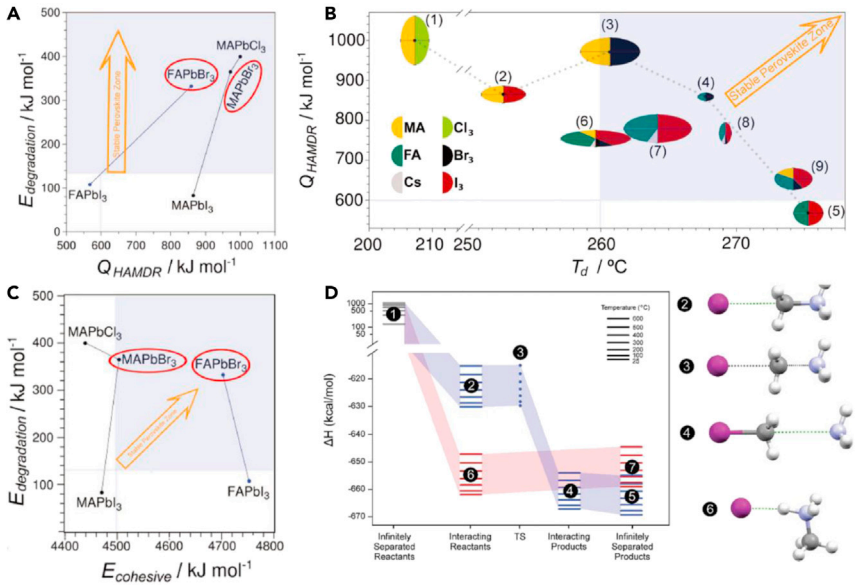

Figure 4. Thermodynamic instability of perovskites

(A) Experimental Q_{HAMDR} versus theoretical $E_{degradation}$ parameters.

(B) Experimental stability map of hybrid halide perovskites described by two parameters T_d versus Q_{HAMDR}.

(C) Theoretical E_d versus theoretical E_c map. Credit adapted from (García-Fernández et al., 2018).

(D) Thermodynamic cycle depicting the decomposition process of MA^+ assisted by I^- for the chemical reaction pathways producing CH_3I and NH_3. Credit adapted from (Wei et al., 2020).

FA^+ cations (Lee et al., 2015; Tan et al., 2018; Yang and Kelly, 2017). Incorporating Cs^+ into perovskite lattice would be advantageous for moisture and light stability with insensitivity toward thermal stress. The high entropy gain in mixed perovskites with enhanced thermal performance can signify a general rule to PSC technology.

Mechanical instability

Mechanical instability in pure perovskites

Due to their soft lattice characteristics, the perovskite, especially organic-inorganic hybrid perovskites, enable adjustable structural and optoelectronic properties via strain regulation. However, they are also subject to mechanical fragility and long-term instability due to their inherent brittle crystal structure (Ma et al., 2021; Rolston et al., 2016). Generally, the different sizes of the organic amines reveal a significant effect on stiffness and softness via bonding the inorganic framework and hydrogen bonding. The hydrogen-bonding induced octahedral tilting can significantly adjust the electronic structure and structural properties. Notably, the effect of mechanical deformation by A-site engineering is negligible compare to the host-guest interaction (Ji et al., 2019; Sun et al., 2017). When discussing the X-site ions, the stiffness decreases as the electronegativity of halogen decrease (Cl^-> Br^-> I^- for electronegativity, respectively). The decreased electronegativity further leads to a reduced Pb-X bond strength in halide perovskites. Sun et al. calculated Young's moduli (E) for $FAPbI_3$ and $FAPbBr_3$ single crystal using the Oliver-Pharr method as demonstrated in Figures 5A–5C (Sun et al., 2017). The two perovskites both showed the anisotropy feature in the stiffness and the stiffest structures along Pb-X-Pb chains aligning along (100) plane unlike the MA-based single perovskites ($MAPbBr_3$ is stiffer than $MAPbI_3$). The bulk modulus (B), shear modulus (G), and E represent the elastic characteristic of the volumetric, shear, and uniaxial deformation, respectively. When changing the interaction energy between MA^+ and PbX_3 by extra strain, Faghihnasiri et al. demonstrated that the greater tolerance factor (close to 1) would have a denser structure (smaller E and B) (Faghihnasiri et al., 2017). A similar trend is also proved by Lee et al (as shown in Figures 5D–5F) (Lee et al., 2018) The MA cations have a greater influence on the elastic properties than other cations depending on the sterility (conformation) and hydrogen bonding interaction. Furthermore, Pb-based halide perovskites have smaller moduli than Sn-based perovskites due to the decreasing B-X bond strength when increasing the size of B- and X-site ions in Pb-based perovskites. The contribution of B- and X-sites for elastic moduli is greater than A-sites.

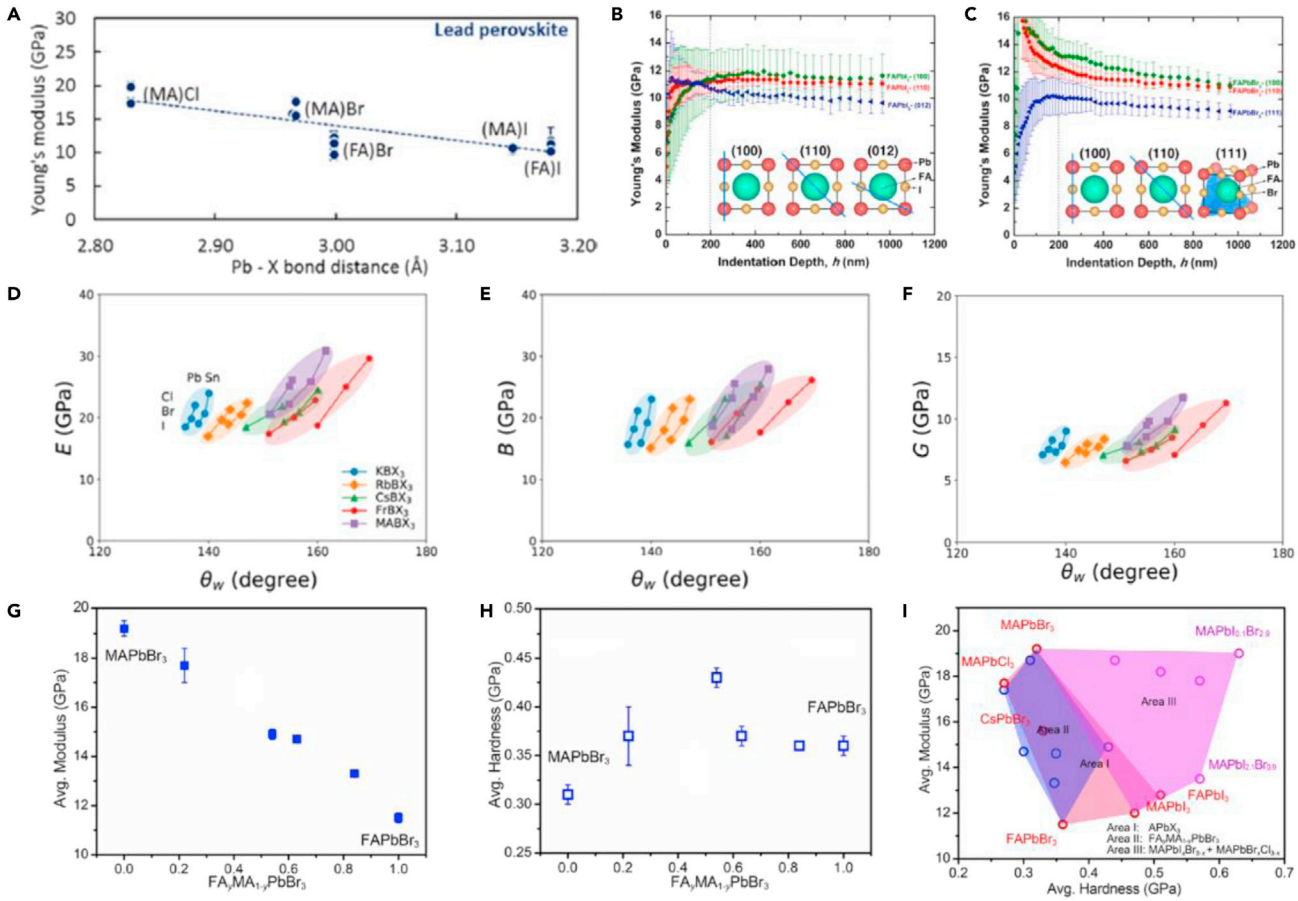

Figure 5. Mechanical properties of perovskites

(A) Young's moduli of hybrid halide perovskites.

(B) Young's moduli of cubic $FAPbI_3$ were conducted on (100), (110), and (012) planes.

(C–H) Young's moduli of cubic $FAPbBr_3$ were conducted on (100), (110), and (111) planes. Credit adapted from (Sun et al., 2017). Effect of chemical substitution on the isotropic polycrystalline elastic moduli of halide perovskites in (D) Young's modulus *E*, (E) bulk modulus *B*, and (F) shear modulus (*G*) Credit adapted from (Lee et al., 2018). The value of (G) E, (H) hardness (*H*) of mixed $FA_xMA_{1-x}PbBr_3$ perovskites.

(I) *H* versus *E* for mixed perovskites. Credit adapted from (Ma et al., 2021).

Mechanical instability in mixed perovskites

To explore the mechanical behaviors in mixed A/X sites, the biggest concern is that the calculated E using DFT, PSEsol or vdW methods are much higher than the experimental results (Faghihnasiri et al., 2017). As far as we know, the fundamental understanding of mechanical stability in A/X sites was first reported by Ma et al. (Figures 5G–5I) (Ma et al., 2021) Due to the hydrogen bonding when mixing the A sites, there was nearly a linear decrease of E when increasing the FA^+ contents (Figure 5G). Similarly, the mixture of A sites also showed an increase of hardness (H) as shown in Figure 5H, which could be ascribed to the lattice distortion of mixed perovskite materials. The origin difference of E with different A sites values contributes to the difference of hydrogen bonding between the X sites and H atoms of the A sites, the dipole moment, and the size of molecules, which could be regarded as a powerful measure to adjust the E in mixed perovskite to apply to different device structures. Adding 5% Cs^+ in A sites with a perovskite structure of $Cs_{0.05}FA_{0.7}MA_{0.25}PbI_3$ would lead to a lattice distortion of inorganic framework and increase the energy barrier for dislocation slip through perovskite, thus increasing the resistance of plastic deformation (Wu et al., 2018). The distribution of E and H values in $MAPbI_xCl_{3-x}$ and $MAPbI_xBr_{3-x}$ perovskites have been significantly enriched and enlarged (Figure 5I). Generally, the low value of E is beneficial for strain relaxation of the interface, especially considering flexible devices. Therefore, the mixture of A/X sites could modulate the ductility of the perovskite materials.

Table 2. Effects of A/X sites regulation in recent high-performance PSCs.

Perovskites	Functional component	Key effect	Year	Refs
$FAPb(I_{0.85}Br_{0.15})_3$	FA^+	The fraction of actively rotating FA molecules is minimized. The 15% Br^- sample was at least ~2 times longer than others.	2020	Johnston et al. (2020)
$Cs_{0.05}(MA_{0.15}FA_{0.85})_{0.95}Pb(I_{0.85}Br_{0.15})_3$	Cs^+	5% Cs^+ is the most robust and electronic structure or valence band edge is least perturbed	2017	Deepa et al. (2017)
$Cs_yFA_{1-y}Pb(Br_xI_{1-x})_3$	Cs^+	Cs^+ substitution stabilizes the lattice to suppress phase segregation	2020	Hao et al. (2020)
$Cs_{0.06}(MA_{0.17}FA_{0.83})_{0.94}Pb(I_{0.83}Br_{0.17})_3$	Cs^+	Cs^+ incorporation suppresses the movement of ions strain	2019	Tennyson et al. (2019)
$FA_xCs_{(1-x)}PbI_3$	Cs^+	Cs^+ incorporation is sufficient to stabilize the perovskite phase with a lower degree of distortion of the host lattice	2020	Boziki et al. (2020)
$MA_{0.95}Cs_{0.05}PbI_3$	Cs^+	Cs^+ incorporation suppresses the formation of reactive superoxide ions (O_2^-) as well as ion migration in perovskites by forming additional energy barriers	2021	Lin et al. (2021)
$MA_{0.5}Cs_{0.5}PbBr_{1.5}I_{1.5}$	Cs^+	Cs^+ incorporation suppresses the halide ion migration and improves the stability	2021	Kamat and Kuno (2021)
$FA_{1-x}MA_xPbI_{2.87}Br_{0.13}$ (Cl)	FA^+, MA^+	The reduction of surface energy for FA^+/MA^+ mixed-cation perovskites result in the preferable crystal orientation	2019	Xu et al. (2019)
$MA_{0.95}GA_{0.05}PbI_3$	GA^+	5% GA substitution suppresses I^- ion transport	2019	Ferdani et al. (2019)
$FA_{0.85}MA_{0.15}PbI_{2.55}Br_{0.45}$	K^+	The incorporation of K^+ prevents the formation of iodide Frenkel defect	2018	Son et al. (2018)
$(FAMACsRb)_{100-x}K_x$	Cs^+, Rb^+, K^+	The incorporation of Cs^+, Rb^+ and K^+ exhibit higher carrier mobility via affecting crystal facet rotation	2018	Zheng et al. (2018)
$FA_{0.83}MA_{0.17}Pb(I_{0.83}Br_{0.17})_3$, adding 5% CsI or RbI	Cs^+, Rb^+	Cs^+ reduces the trap density and Rb^+ increases the charge carrier mobility	2018	Hu et al. (2018)
$FA_{1-x}MA_xPb(I_{3-x}Br_x)$, adding RbI and CsI	Cs^+, Rb^+	The incorporation of Cs^+ and Rb^+ result in enlarged homogeneous grain size with minor modification of unit cell	2020	Patil et al. (2020)
$(MAFA)_{0.9025}(CsI)_{0.0475}(RbI)_{0.05}$	FA^+, MA^+, Cs^+	The incorporation of FA^+, MA^+, Cs^+ yield increased perovskite grain size and prolonged charge carrier lifetimes	2019	Solanki et al. (2019)
$(FA_{0.83}MA_{0.17})Pb(I_{0.83}Br_{0.17})_3$, adding 7% Cs^+ and 3% Rb^+	FA^+, MA^+, Cs^+, Rb^+	These components enable the uniform distribution of halides, which in turn prevents the formation of isolated halide- and cation-rich phases	2019	Dang et al. (2019)
$Cs_xMA_{0.05-x}FA_{0.94}Pb(I_{0.99}Br_{0.01})_3$	Br^-	Br^- incorporation is beneficial to enhance the stability of $FAPbI_3$-based PSCs via suppressing the trap density in perovskite films.	2020	Xie et al. (2020)
$MAPb(Br_{0.5}I_{0.5})_3$	Br^-, I^-	Halide vacancies/interstitials are a charged and highly mobile defect	2020	Knight et al. (2020)
$Cs_{0.05}MA_{0.15}FA_{0.8}PbI_{2.55}Br_{0.45}$	Cs^+, Br^-	The incorporation of Cs^+ and Br^- induces inhomogeneous crystallization	2020	Saidaminov et al. (2020)
$(MA/FA/Br)Pb(I/Br)_3$	Cs^+, MA^+, Br^-	Cs^+ helps prevent decomposition into precursors, Br^- mixing is the most effective method of stabilizing the desired α-phase; MA^+ mixing is moderately effective at stabilizing the α-phase, it is useful in minimizing the Br content required for α-phase stabilization.	2020	Kim et al. (2020b)

A/X SITES COMPONENT ALLOYING

The introduction of different cations/ions at A/X sites of metal halide is a great method to tune their optoelectronic properties and long-term stability. Here, we mainly discussed A/X sites component alloying based on band gap regulation, charge-carrier dynamics, ion migration and hysteresis, crystallinity and phase control, residual control, and stoichiometric control. The strategies of using A/X sites in hybrid perovskites and their effect on photoelectric property gives a detail summarized in Table 2.

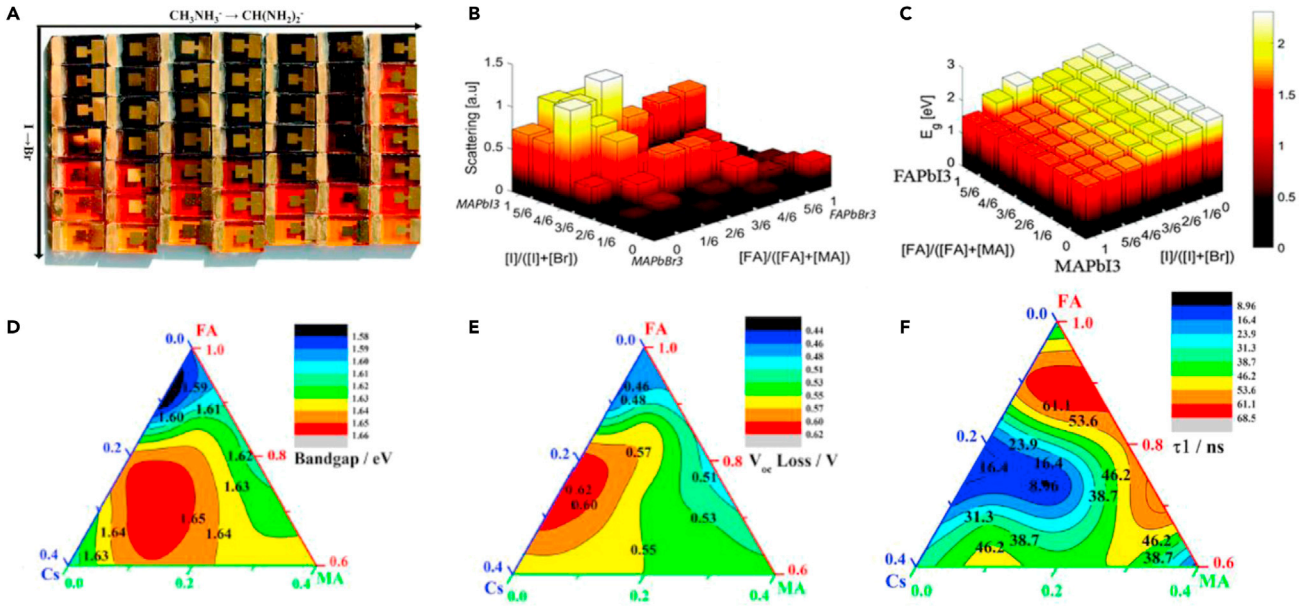

Figure 6. Bandgap regulation in perovskite

(A) A photo of PSCs with a different compositional ratio of A site and X site.

(B and C) Illustration of (B) absorption and (C) band gap for different compositional spaces. Credit adapted from (Jesper Jacobsson et al., 2016).

(D–F) The band gap, (E) V_{oc} loss, and (F) PL lifetime (τ_1) as a function of ternary MA^+, FA^+, and Cs^+ compositions. Credit adapted from (Li et al., 2017).

Band gap regulation

The valence band (VB) of ABX_3 halide perovskites is composed of the long pair Pb 6*s* and halide *p*-orbital with strong anti-bonding interaction, while the conduction band (CB) is derived from Pb 6*p* and halide *p*-orbital with weak anti-bonding interaction (Umebayashi et al., 2003; Yin et al., 2015). The typical band gap is around 1.2 ~ 2.4 eV for multi-component perovskites, which would be ideal absorbers in single- or multi-junction solar cells (Brennan et al., 2017). Generally, the A-site cations evolved from single MA^+ or FA^+ to dual cations of MA^+/FA^+, MA^+/Cs^+, and FA^+/Cs^+, and further to ternary cations of $Cs^+/MA^+/FA^+$. Meanwhile, the X site varied from I^- anion to I^-/Cl^- or I^-/Br^- anions. The Pb^{2+}/Sn^{2+} alloying in B sites could further adjust the band gap to infrared range, favoring all-perovskite tandem devices. For this part, we will focus on the reported component alloying to afford a diverse family of multi-components with tailorable band gap properties under the tolerance factor rule.

Generally, the optical and electronic performance of $APbI_3$ perovskites could be tailored through altering lattice parameters (e.g., lattice contraction or dilation of Pb-X lattice) or octahedral tilting (Amat et al., 2014). The magnitude of the band gap is highly correlated to the Pb-I-Pb angle (Amat et al., 2014; Chen et al., 2015c). Due to the higher probability of hydrogen bonding formation of FA^+ cations compared to MA^+ cations, the spin-orbit coupling can be enhanced in pseudocubic $FAPbI_3$ perovskites by increasing the ionic feature of Pb-I bonding and Pb character in the CB location. Jacobsson et al. explored 49 different perovskite compositions via gradually replacing MA^+ to FA^+ and I^- to Br^- (as shown in Figure 6A), thus inducing a remarkable PCE up to 20.7% (Jesper Jacobsson et al., 2016). The exchange of organic cations had negligible effects on the density of the state. The semitransparency as depicted in Figure 6B reflected that the high scattering was distributed in the middle of the matrix and the pure iodide perovskites. Meanwhile, the band gap in Figure 6C gradually increased when replacing I^- to Br^-, and showed only 0.7 eV difference between pure iodide and bromide perovskites. As proved, due to the C 2*p*, N 2*p* and H 1*s* orbital do not contribute to state density closed to E_f, the A site cations have little influence on band gap. However, MA^+ or FA^+ cations can perturb halide scaffold by van der Waals interaction and hydrogen bonding (Lee et al., 2016; Svane et al., 2017). The H atoms in FA^+ cations contact with I^- ions closely in mixed cation systems due to strong cage tilting, thus forming strong N-H ··· I interaction and hydrogen bonding(Ghosh et al., 2017)Cs^+ has a remarkable chemical and thermodynamic stability than other organic cations. A small amount of Cs^+ has been proved to stabilize phase structure via increasing configurational entropy and locking $(PbX_6)^{4-}$ octahedral tilting. Cs^+ tends to remove the detrimental deep traps, or else shift traps closer to

CB or VB (Jin et al., 2020a). By combining mixture design (MD) methods, Zhou et al. revealed the composition-property relationship and synergistic effects among (Cs, FA, MA)PbX_3 perovskites (Li et al., 2017). A band gap variation from 1.56 to 1.65 eV appeared when adjusting multi-components in the tertiary space (Figure 6D). The highest band gap value is composed of 26.7% Cs^+, 6.6% MA^+, and 66.6% FA^+, while it appears a small increase when Cs^+/MA^+ incorporating in FA-based perovskites within certain limits. Considering the V_{oc} loss in Figure 6E around 60 mV from the theoretical limit (Liu et al., 2019), the low V_{oc} loss mainly centers on the FA-based perovskites with a small concentration of either MA^+ or Cs^+. Correspondingly, the surface recombination (τ_1) rather than bulk recombination (τ_2) is more relevant to V_{oc} loss, thus inferring that surface/interface recombination is more correlated to the device performance in PSCs (Figure 6F). Among triple-cation perovskites, the best PCE has reached 23% by Cs^+/FA^+/MA^+ mixing (Table 1) (Zheng et al., 2020) Subsequently, Snaith et al. fabricated $FAPb(I_xBr_{1-x})_3$ mixed perovskite and showed a gradual red-shift band gap when increasing I^- fraction (Eperon et al., 2014).

Indeed, the A site alloying could tune the band gap, improve the charge-carrier mobility, and enhance the optoelectronic properties by modifying the organic framework and octahedral inorganic framework. However, the lattice strain effect and chemical pressure by Cs^+-FA^+ alloying in halide perovskites would strongly affect the structural distortion as well as the rotational motion of FA^+ and dynamic tilting of $(PbI_6)^{4-}$ octahedral framework. This phenomenon can give rise to Rashba defect, inducing an indirect band gap via removing the electron spin degeneracy and splitting each of the band edges of CB and VB (Kepenekian et al., 2015; Stranks and Plochocka, 2018). The band gap transition from direct to indirect also plays a key role in reducing the charge carrier recombination in hybrid perovskites.

The general X site is halide anions (e.g., Cl^-, Br^- and I^-) in the halide perovskite structure. Halide transition has a significant effect on VB and follows the order of 3*p* to 4*p* and then to 5*p* with the halide variation from Cl^- to Br^- and then to I^-(Brivio et al., 2013). The photovoltaic absorption capacity can be adjusted by multi-X site structure. The band gap of $MAPb(I_xBr_{1-x})_3$ has a gradual switch within 1.6–2.3 eV(Ippili et al., 2018; Unger et al., 2017), while $MAPbI_3$ has achieved a V_{oc} up to 1.18 V (Wang et al., 2018a). Seok et al. used a 4-state model to give a thermally relaxed emission process from $MAPbI_{3-x}Cl_x$ perovskites (Park et al., 2017). Compared to pure $MAPbI_3$ perovskites, the band gap grading effect showed a decreased tendency for $MAPbI_{3-x}Cl_x$ perovskites. The hole concentration at back contact and back contact recombination was decreased The X^- mixing in halide perovskites has a crucial role to achieve optimum band gap for tandem device application. Xu et al. used triple-halide alloying to tailor the band gap and achieved a PCE of 27% in two-terminal monolithic tandem PSCs (Xu et al., 2020). Snaith et al. reported that the V_{oc} loss was dominated by the low initial radiative efficiency of mixed perovskites and the corresponding devices fail to deliver the expected V_{oc} due to terrible halide segregation (Mahesh et al., 2020). By maximizing the initial radiative efficiency, a device with $FA_{0.83}Cs_{0.17}Pb(I_xBr_{1-x})_3$ (40% Br^-, band gap for 1.77 eV) showed a slight 75 mV dropping in V_{oc} even halide segregation occurs. Therefore, improving the radiative efficiency of alloyed perovskites and exploiting an efficient perovskite/CTL (charge transport layer) interface should be pursued.

Charge-carrier dynamics

The superior physical and chemical properties of perovskites such as long carrier diffusion length (>1 μm), high light absorption coefficient (around 10^5 cm^{-1}), and high defect tolerance can be easily tuned via varying chemical compositions in the precursor. Under the real operation of PSCs, the perovskites harvest the incident photons and then convert to free charge carriers (electron and hole) by a built-in potential field. The electrons and holes are collected by cathode and anode after diffusion, transport, and extraction processes (Li et al., 2020). However, the nonradiative recombination including Shockley-Read-Hall (SRH) recombination, Auger recombination, and surface/interface recombination occurred along with defects, impurities, phonons, and mobile species (Kirchartz and Rau, 2017; Merdasa et al., 2019). Knight et al. identified three defect types (MA^+ interstitials, halide vacancies/interstitials, and crystal distortions, respectively) and their effects on $MAPb(Br_{0.5}I_{0.5})_3$ perovskites (Figures 7A and 7B) (Knight et al., 2020) The photoluminescence (PL) behavior showed no significant changes under 0–1 V applied bias (Figure 7A). Meanwhile, the PL peak of I^--rich phase (integrated within 720–770 nm) and mixed-halide phase (integrated within 640–690 nm) showed increased and decreased intensity, respectively, indicating that the photo-excited charge carrier would funnel from the mixed-halide phase into I^--rich phase. The PL signal of mixed-halide regions showed decreased tendency relative to I^--rich phase, indicating that the different illumination intervals have considerable effects on the amount of halide segregation. Notably, the halide

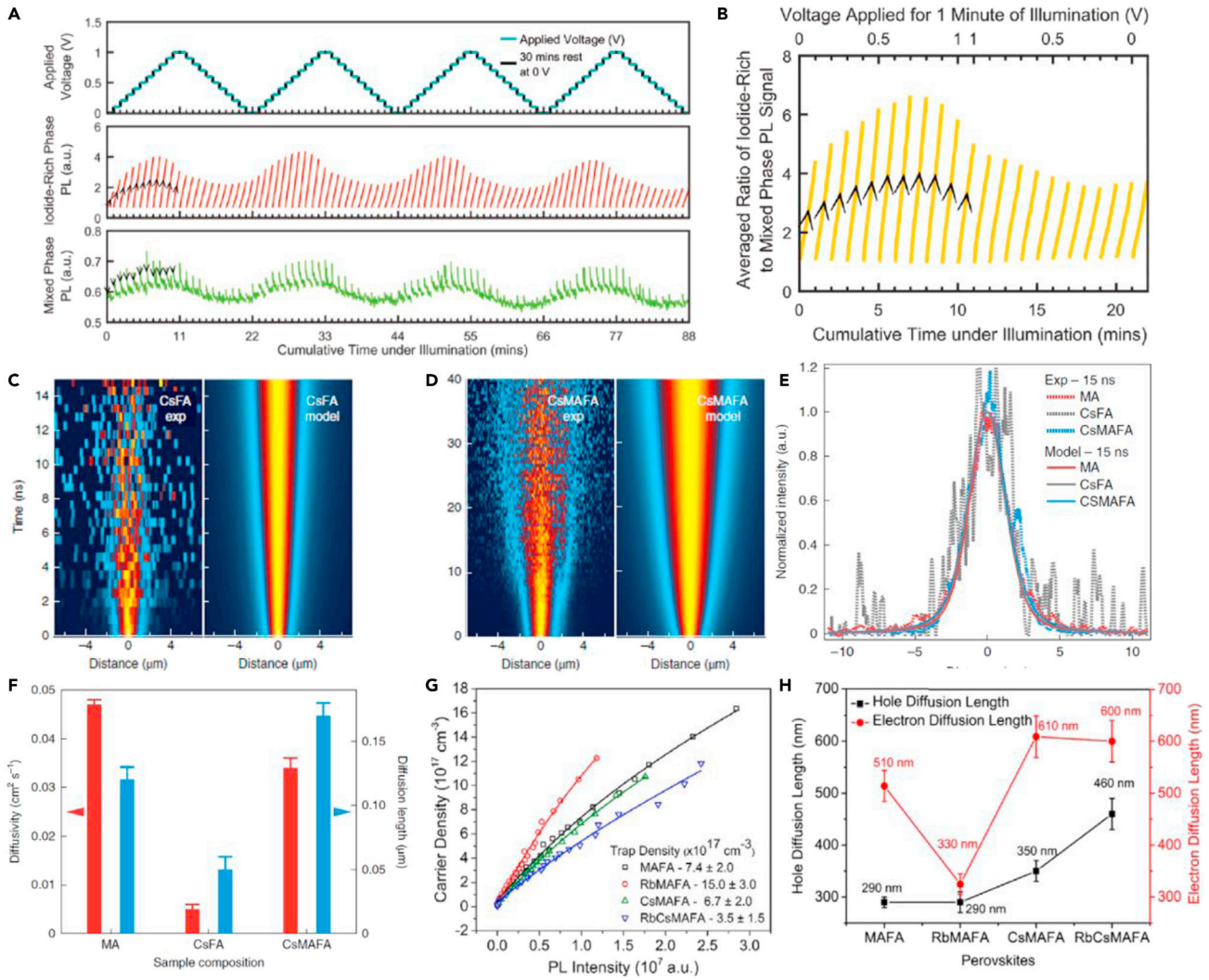

Figure 7. Charge-carrier dynamics of perovskites

(A) PL and extracted current measurements from a mixed-halide perovskite device as an applied voltage across the device is repeatedly ramped up and down between 0 and 1 V. Top panel: The voltages applied across the device and indication of the rest intervals during the experiment. Middle panel: The integrated low energy PL (720–770 nm) from the device under 400 nm, 110 mW cm^{-2}, continuous-wave illumination. Bottom panel: The integrated higher energy PL (640–690 nm) from the device.

(B–D) The ratio of the PL signals from the middle and bottom panels of (A). Credit adapted from (Knight et al., 2020). Normalized experimental and simulated carrier diffusion patterns for (C) CsFA-based films and (D) CsFA-based crystals.

(E and F) Experimental and simulated carrier diffusion and (F) diffusivity (red bars) and diffusion lengths in all single crystals. Credit adapted from (Saidaminov et al., 2020).

(G and H) Photoexcited carrier density and (H) the impact of different cations on electron and hole diffusion lengths in different perovskite films. Credit adapted from (Solanki et al., 2019).

segregation always takes place in the region of the I^--rich phase due to the limited amount of spatial freedom with a high radiative recombination rate. Interestingly, the MA^+ interstitials, deemed to a mobile trap state, could reduce the quantity of charge carriers captured in neutral defects states, thus suppressing halide segregation.

Afterward, Sargent et al. implied the competing carrier diffusivity processes in crystals and thin films with six components ($Cs_xFA_yMA_{1-x-y}PbI_zBr_{3-z}$) using transient photoluminescence microscopy (TPLM) technology as demonstrated (in Figures 7C–7F and Table 2) (Saidaminov et al., 2020) For carrier diffusion, it was not affected in single crystals but thin films under component variation in A sites (Figures 7C and 7D). The

full-wavelength at half maximum (FWHM) of CsFAMA-based single perovskite crystal was four times larger than that of the thin films. Conversely, there was no obvious difference after temporal evolution for MA-, CsFA-, and CsFAMA-based single crystals both in calculated and experiment results. Distinguishingly, MA^+-based films showed ~0.047 $cm^2\ s^{-1}$ carrier diffusivity, while FA^+-Cs^+ mixed films showed an order of magnitude decreased diffusivity in Figure 7F. Residual FA^+ and halides also contribute to increased trap-assisted charge recombination and decreased diffusion length (Figures 7G and 7H) (Solanki et al., 2019) Interestingly, incorporating MA^+ in FA^+-Cs^+ films leads to uniform grain composition, allowing ~0.034 $cm^2\ s^{-1}$ diffusivity. Chen et al. reported a mixed perovskite of $(FAPbI_3)_{0.9}(MAPbBr_3)_{0.05}(CsPbBr_3)_{0.05}$ with high structural stability. The corresponding PSC device exhibited outstanding thermal stability, including 10,000 h moisture stability and 1000 h light stability (Chen et al., 2019a).

As reported in the radiative limit, the indirect band gap perovskites show smaller absorption coefficients and lower charge mobilities than direct transition (Kirchartz and Rau, 2017). Ghosh et al. observed a higher Rashba-type spin-splitting in $FA_{0.75}Cs_{0.25}PbI_3$ than pure $FAPbI_3$ perovskite (Ghosh et al., 2018). Meng et al. demonstrated that the Br^--containing pure perovskites possessed dual exciton states dominated by excitons, not free carriers (Shi et al., 2020). Levine et al. proved that mixed A/X sites with a structure of $(FA_{0.85}MA_{0.1}Cs_{0.05})Pb(I_{0.83}Br_{0.17})_3$ did not detect deep trap states by surface photovoltage spectroscopy (SPS) and deep-level transient spectroscopy (DLTS) techniques (Levine et al., 2019), which indicated that A/X sites alloying would be a promising channel to decrease defect level and optimize band level alignment. Based on the energy band structure and charge species in hybrid perovskites, there are several origins to explain the dual emission band such as mixed charge species within the perovskites in (e.g., free carrier, free and bound exciton) (Shi et al., 2020; Wu et al., 2019).

Besides, other alternative cations (like rubidium, Rb^+) have also been incorporated in the halide perovskites. For instance, $(MAFA)_{0.9025}Cs_{0.0475}Rb_{0.05}PbI_3$ perovskites (simplified as RbCsFAMA) were deposited and 20% PCE was obtained by suppressing defect density with increased carrier diffusion length(Solanki et al., 2019). The Cs^+ in RbCsFAMA perovskites, in return, passivate trap states effectively, therefore getting balanced and enlarged electron/hole diffusion length (d_e = 600 nm and d_h = 460 nm). Hu et al. also added Rb^+ into MA^+-FA^+-Cs^+ perovskite to reduce the second-order compound rate of the free carrier in the bulk (Hu et al., 2018). The thermally stimulated current (TSC) images revealed a wide distribution of trap state energy for pristine MAFA-based devices while introducing small amounts of Rb^+ induced a deeper trap state. The quadruple cations showed electron mobility of 15 $cm^2\ V^{-1}\ s^{-1}$ and hole mobility of 16 $cm^2\ V^{-1}\ s^{-1}$, almost a half increase compared to dual-cations perovskite. Besides, adding Rb^+ could suppress the growth of PbI_2 via forming $RbPbI_3$(Matsui et al., 2018). Matsui et al. proved that a small Br^- ratio of 5% in $(Rb_{0.05}Cs_{0.05}FA_{0.75}MA_{0.15}Pb[I_{0.95}Br_{0.05}]_3)$ enabled the best initial PCE of 20.1% and state-of-the-art thermal stability under 85% RH and 85°C heating tests for 1000 h (Matsui et al., 2019). Interestingly, a slightly high ratio of Br^- in $(Rb_{0.05}Cs_{0.05}FA_{0.75}MA_{0.15}Pb[I_{0.83}Br_{0.17}]_3)$ had non-negligible decreased efficiency at 85°C heating for 600 h. The Br^- and Rb^+ agglomerates in the plane direction were presented after the thermal stress test. The Rb and Br signals were also observed through energy-dispersive X-ray spectrometry (EDX) tests, which were similar to the phase-separated compounds like $Rb_xPb_yBr_z$, $RbI_xBr_{1-x,}$ or KBr(Abdi-Jalebi et al., 2018; Kubicki et al., 2017). The alkali metals generally occupy interstitial sites instead of incorporating to perovskite lattice, showing alleviated ion migration and negligible hysteresis. Son et al. proposed that the Frenkel defect of I^- in $MAPbI_3$ could easily be formed due to ion migration from lattice to interstitial site (Son et al., 2018). The spatial location of excess electrons was localized closed to Pb and I vacancy (V_I), which stabilized the Frenkel defect of I^- via Pb-V_I-Pb spatial arrangement. K^+ doping showed a stronger effect on mixed perovskite (such as $FA_{0.875}MA_{0.125}PbI_{2.55}Br_{0.45}$) than pristine perovskite (such as $FAPbI_3$ and $MAPbI_3$). The structural distortion deriving from the shape difference between MA^+ and FA^+ accommodates K^+ into the interstitial site easily, therefore lowering the defect formation energy of K^+ interstitial in mixed cation perovskites. Notably, the cation/anion ratio of K^+/I^- was 0.616, fitting well into the interstitial site and effective coordination interaction. The alkaline cations, despite non-A-site cations in the lattice, could also be added alongside other cation additives (Correa-Baena et al., 2019; Son et al., 2018).

Ion migration and hysteresis

Halogen migration in perovskite generally links to severe current density–voltage (J-*V*) hysteresis in PSCs devices (Chen et al., 2015a; Mosconi and De Angelis, 2016). I^- migration shows faster velocity than MA^+ and Pb^{2+} (Eames et al., 2015). Meggiolaro et al. disclosed that the migration energy barrier of interstitial I^- (I_i) was higher than I^- vacancy (Meggiolaro et al., 2018). Amphoteric I_i associated with p-doping by I_2

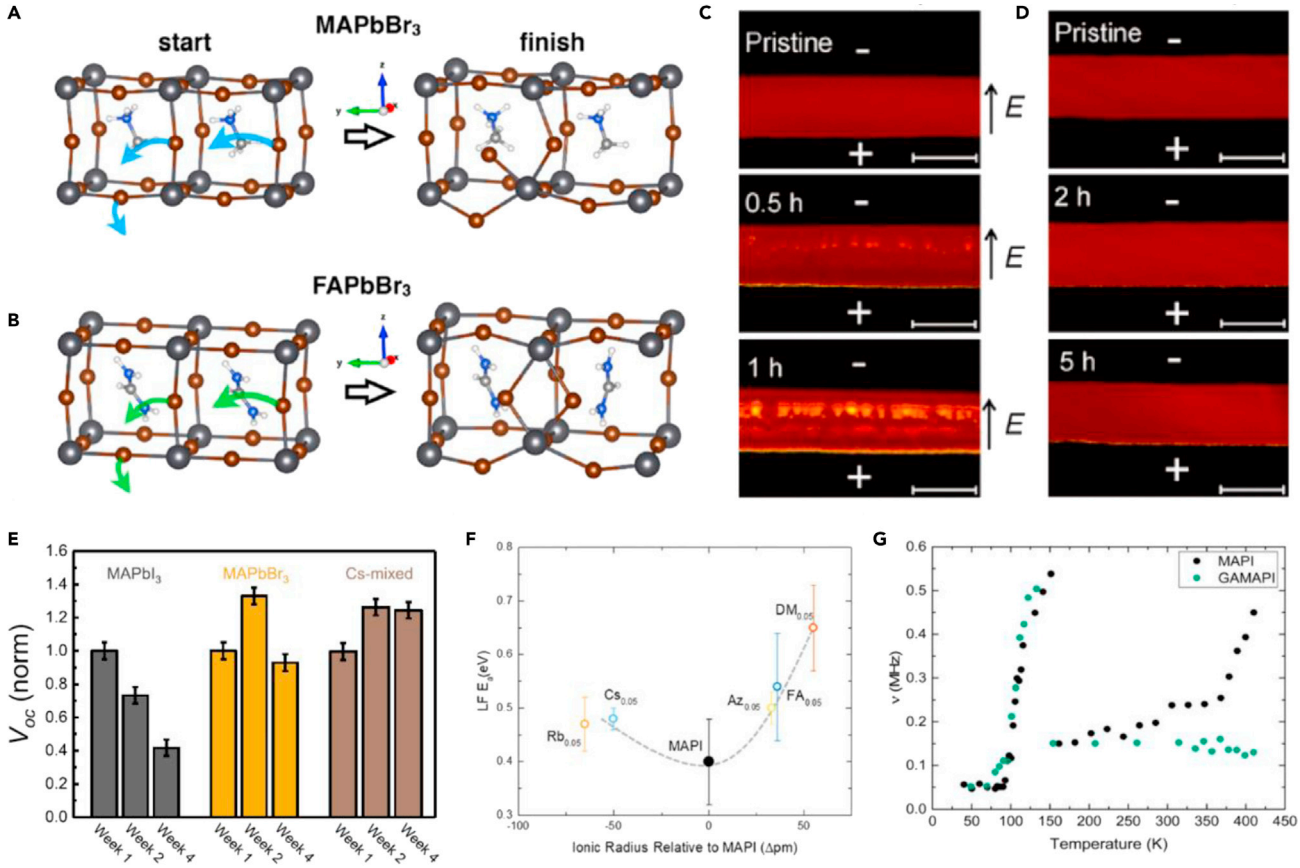

Figure 8. Ion migration in perovskites

(A–D) Illustration of Frenkel V_{Br}—I_{Br} pair migrations and (B) their migration energy profiles in $MAPbBr_3$ and $FAPbBr_3$. Credit adapted from (Oranskaia et al., 2018). Photos of lateral (C) $MAPbI_3$ and (D) $MA_{0.95}Cs_{0.05}PbI_3$ devices during the same OP-decay processes under 0.2 V μm^{-1}applied bias. Credit adapted from (Oranskaia et al., 2018).

(E) Histograms of V_{oc} for three different perovskites testing over 4 weeks. Credit adapted from (Tennyson et al., 2019).

(F) The activation energy plot against the A-cation ionic radius relative to MA^+.

(G) Temperature dependence of fluctuation rate for $MAPbI_3$ and $MA_{0.95}GA_{0.5}PbI_3$ perovskites. Credit adapted from (Ferdani et al., 2019).

vapor could trap electron-hole pairs under light irradiation. In pure Br^--containing perovskite, Oranskaia et al. exposed that the $FAPbBr_3$ scaffold had a higher rotation barrier and formation energy than $MAPbBr_3$(Oranskaia et al., 2018). The minimum energy migration barriers in Figures 8A and 8B showed a Br^- vacancy (V_{Br}) of 0.27 V and a Br^- interstitials (Br_i) of 0.34 eV for $MAPbBr_3$, and a V_{Br} of 0.33 eV and a Br_i of 0.24 eV for $FAPbBr_3$, respectively, which revealed stronger H-bonding stabilization and higher rotation barrier in FA^+. The Frenkel V_{Br}-Br_i pair migration barriers showed much higher intensity than V_{Br} and Br_i, indicating that defect intensity not only occurs in crystal growth but also in Frenkel pair formation. In I^--Br^- mixed halide perovskite, the energy depth of the recombination center decrease with increasing I^- content. In particular, the Urbach energy is mainly related to grain surface-to-volume ratio (e.g. grain size) in halide-decided components, thereby indicating the crucial role of grain boundary (GB) (Fedeli et al., 2015). The defect state at GB strongly affects sub-bandgap absorption. Therefore, identifying the migration channel mediated by grain bulk or GB and the corresponding energy barrier could provide a fundamental understanding of the device stability.

The MA^+ and I^- in pure perovskites can easily migrate under an electric field due to the Frenkel defect pairs (e.g., interstitial and vacancy defect) (deQuilettes et al., 2016). Yuan et al. found incorporated 5% Cs^+ could stabilize perovskite lattice, thus suppressing the formation of O_2^- by inducing an additional energy barrier (Figures 8C and 8D) (Lin et al., 2021). By configuring a lateral device with a structure of Au/perovskite/Au, the oxygen and photo-induced decay results illustrated that the regions adjacent to Au electrodes start

decomposition with the appearance of I^- vacancy. Oxygen molecules tend to reside in I^- vacancy and form electron traps as well as the photo-generated O_2^-. As an opposite trend, the lateral device with $MA_{0.95}Cs_{0.05}PbI_3$ perovskites showed no obvious decomposition with external bias, indicating robust protection of Cs^+ incorporation on photo-oxygen stability. Therefore, inorganic Cs^+ could rigidize the pure $MAPbI_3$ perovskite lattice, thus suppressing the anharmonic motion of MA^+. Meanwhile, Tennyson et al. proved that the $Cs_{0.06}(MA_{0.17}FA_{0.83})_{0.94}Pb(I_{0.83}Br_{0.17})_3$ perovskites are electrically uniform in macro- and nanoscale and low V_{oc} dropping week-after-week is observed (Figure 8E) (Tennyson et al., 2019) Apart from above-mentioned A-site cations, Ferdani et al. used muon spin relaxation (μSR) to probe detect transformation of nuclear dipole field arising from moving ions in Figures 8F–8G (Ferdani et al., 2019). 5 mol% GA^+ (guanidine) substitution could increase the activation energy for I^- migration. The observed fluctuation rate showed a decreased tendency over 150 K, which implies a phase transition tuning from orthorhombic to tetragonal. MA^+ actions would reorient within lattice when closing to 140 K (Leguy et al., 2015a).

Crystallinity and phase control

The crystallization dynamics for mixed halide perovskites depend strongly on the interfacial energy anisotropies and kinetic attachment for different chemical compositions (Sanchez et al., 2021). Rapid crystallization processes could result in dendrite growth, wherein the diffusion processes further control the phased transformation rate. Establishing a relationship between A/X site components and crystal preferential growth is crucial.

Crystallization dynamics with A/X sites modulation

In 2016, Grätzel et al. investigated the mixed cations and halides with $Cs_{0.05}(MA_{0.17}FA_{0.83})_{0.95}Pb(I_{0.83}Br_{0.17})_3$ formulation (Saliba et al., 2016). Cs^+ contributed to the beneficial α phase of FA^+ and well-tuned Goldschmidt tolerance factor (Li et al., 2016). For typical ABX_3 hybrid perovskites, Zhou et al. guided the crystal stacking mode by an A-site cation cascade (Zheng et al., 2018). In particular, the cation cascade (from MAFACs, MAFACsRb, to MAFACsRbK) in perovskites showed crystal facet rotation along with out-of-plane and in-plane directions. The preferred orientation leads to a specific rearrangement of $[PbI_6]^{4-}$ octahedral framework (Figures 9A–9B), reducing corresponding chemical potential to form more thermodynamically stable thin films. Afterward, Zhou et al. optimized the components with the formula of $(FA_{1-x}MA_x)PbI_{2.87}Br_{0.13}[Cl]$ and delivered a PCE of over 21% (Xu et al., 2019). The preferred crystal orientation along the (001) plane significantly affects charge transportation and collection processes. Similarly, Merten et al. enhanced the black phase purity from 45% in FAMA-based perovskite to 97.8% in CsFAMARb-based perovskites (Figure 9C) (Merten et al., 2021) Cl^- ions in perovskite alloys have admitted to promoting grain growth and slowing down the ratio of grain formation (Chen et al., 2015b; Kim et al., 2019b; Lyu et al., 2020; Wang et al., 2020a). Syed et al. demonstrated the strong saturable absorption peak of 395 nm as well as the reverse saturable absorption peak of 790 nm (two-photo absorption) and 1200 nm (three-photo absorption) in the mixed triple cation halide perovskite (Syed et al., 2020). Strong three-photo absorption near to the band gap reveals optical stabilization, great spatial confinement, and large penetration depth, which is rooted in phonon-assisted anti-Stokes processes(Minda et al., 2018).

The phase fraction of 4H polymorph and PbI_2 phase in FAMA-based perovskites showed a large amount of contribution, which is detrimental to the devices and acts as a trigger to the formation of photoinactiveδ phase. Interestingly, the addition of Cs^+ and Rb^+ indicated a beneficial effect on the suppression of the 4H and PbI_2 phase, enabling a high-purity cubic phase of perovskite films. Meanwhile, the PbI_2 content is higher near the surface than in the bulk, and the hexagonal phase of $FAPbI_3$ shows almost equal contribution both in the bulk and the surface. The FA^+ substituting by smaller Cs^+ or Rb^+ could cause reduced cell volume with tilted $(PbI_6)^{4-}$ corner-sharing octahedral in a larger angle (Ghosh et al., 2017). The role of mixed cations in crystallization dynamics could be attributed to the homogeneous distribution of halogens, thus permitting carriers to move lightly from grain to grain. Rehman et al. established crystal phase-photostability-optoelectronic properties of mixed A/X sites (Figures 9D and 9E) (Rehman et al., 2017) First, they added the Cs^+ cations in a region of 0~0.8, where the FWHM of the (100) plane showed the minimum value with 20% Cs^+ addition. Accordingly, the highest crystalline $Cs_{0.2}FA_{0.8}Pb(Br_{0.4}I_{0.6})_3$ perovskite showed the highest charge-carrier mobility ($18 \pm 2\ cm^2\ V^{-1}\ s^{-1}$) and time-resolved PL lifetime (Figure 9D). Whereafter, they elaborated the value of FWHM, charge-carrier mobility and diffusion length in $Cs_{0.17}FA_{0.83}Pb(Br_xI_{[1-x]})_3$ perovskites to investigated the effects of intrinsic interactions with phonons. They occurred obvious charge-carrier scattering in PL mission linewidth and a continuously decreased mobility with Br^- increasing.

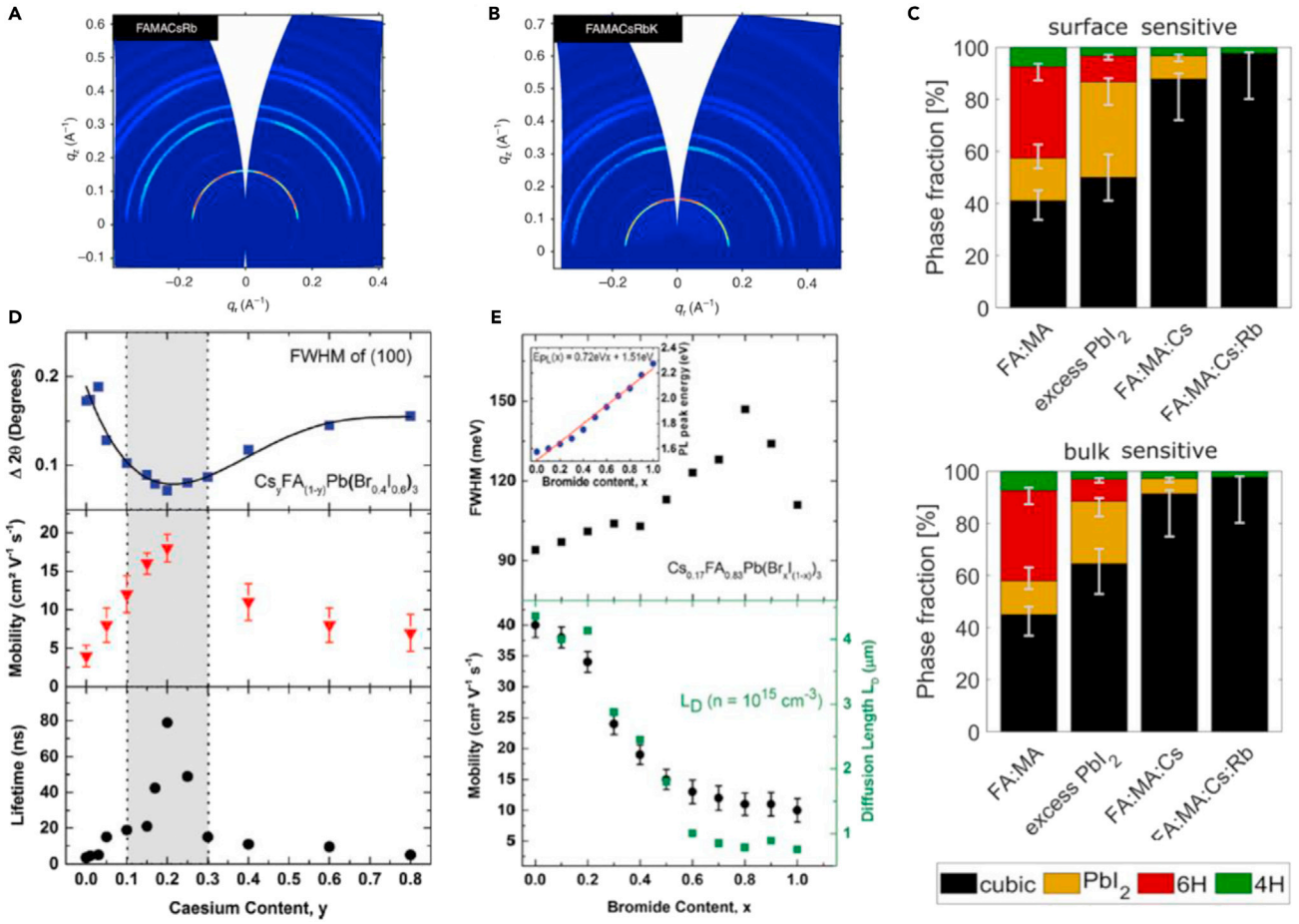

Figure 9. Crystallization dynamics of perovskites

The grazing incidence wide-angle X-ray scattering (GIWAXS) patterns for perovskite films with cation cascade doping as (A) FAMACsRb, and (B) FAMACsRbK, respectively. Credit adapted from (Zheng et al., 2018). (C) Molar phase fractions of cubic, hexagonal, and PbI_2 phases depend on the film composition. Credit adapted from (Merten et al., 2021). (D) Top panel: Shift of the cubic (100) reflection peak in $Cs_yFA_{(1-y)}Pb(Br_{0.4}I_{0.6})_3$ perovskite with varying Cs^+ content ($0 < y < 0.8$). Bottom panel: absorbance onset values and PL peak positions in $Cs_yFA_{(1-y)}Pb(Br_{0.4}I_{0.6})_3$ perovskite with varying Cs^+ content ($0 < y < 0.8$). Credit adapted from (Rehman et al., 2017).

The I^- rich films in $Cs_{0.17}FA_{0.83}Pb(Br_xI_{[1-x]})_3$ perovskites ($0 < x < 0.2$) reached the highest charge-carrier mobility (34–40 $cm^2\ V^{-1}\ s^{-1}$), improving by 50% comparing to $FAPbI_3$ (27 $cm^2\ V^{-1}\ s^{-1}$) in Figure 9E.

Suppressed phase segregation with A/X sites modulation

Suppressed halide segregation in mixed perovskites. Regarding the halide segregation and their ion pathway under prolonged illumination, Brivio et al. observed that the mixture of Br^- in $MAPbI_{1-x}Br_x$ perovskite ($0.3 < x < 0.6$) was subjected to spinodal decomposition and phase segregation at room temperature (Sedighi et al., 2016). The structure with $MAPb_IBr_2$ and $MAPbI_{0.5}Br_{2.5}$ showed stable order, which minimized internal strain due to the size mismatch between Br^- and I^-. Knight et al. demonstrated the link between I/Br segregation and multi A site components in $MAPb(I_{0.5}Br_{0.5})_3$ and $FA_{0.83}Cs_{0.17}Pb(I_{0.6}Br_{0.4})_3$ perovskites (Figures 10A and 10B) (Knight et al., 2021). On the one hand, the *in situ* PL patterns confirmed that the I^- rich region in $MAPb(I_{0.5}Br_{0.5})_3$ perovskites as shown in Figure 10A contributed to the majority of PL emission even though occupying a small fraction of total perovskite volume. The observed phase segregation also resulted in compositional changes based on *in situ* XRD data. On the other hand, the (220) XRD peak of compositionally stable $FA_{0.83}Cs_{0.17}Pb(I_{0.6}Br_{0.4})_3$ perovskites shifted to higher angles after 6 h illumination (Figure 10B), indicating a large ion rearrangement overall volume. The PL and XRD peaks both shifted to lower Br^- content with a broad trend. Therefore, the $FA_{0.83}Cs_{0.17}Pb(I_{0.6}Br_{0.4})_3$ perovskites show

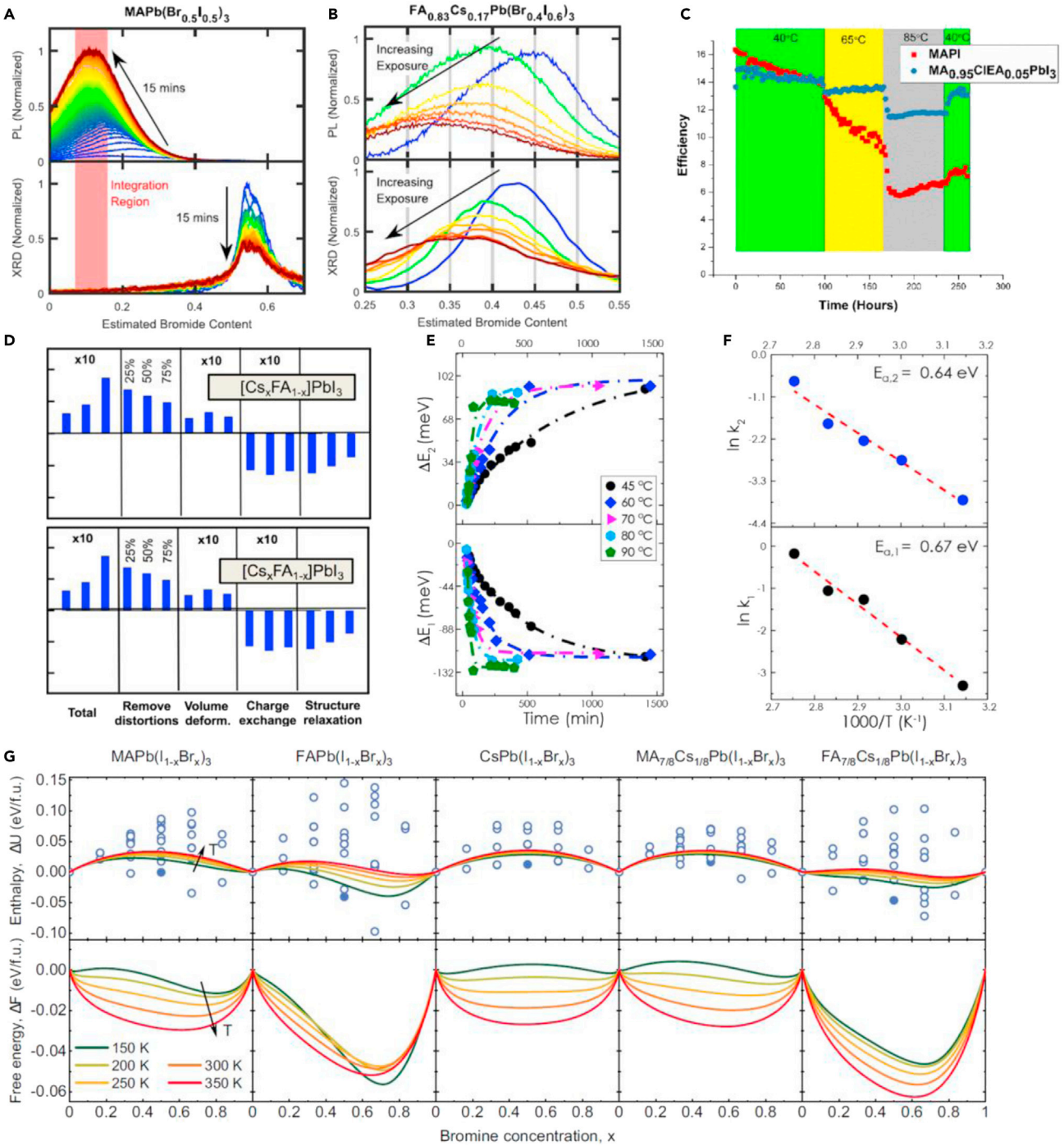

Figure 10. The effect of phased segregation in perovskties

(A) PL spectra and XRD patterns for an $MAPb(Br_{0.5}I_{0.5})_3$ thin film recorded over 15 min illumination.

(B) PL spectra and XRD patterns for an $FA_{0.83}Cs_{0.17}Pb(Br_{0.4}I_{0.6})_3$ thin film recorded over 6 h illumination. Credit adapted from (Knight et al., 2021).

(C) Normalized stability tests of $MAPbI_3$ and $MA_{0.95}ClEA_{0.05}PbI_3$ devices. Credit adapted from (Shirzadi et al., 2019).

(D) Variation of decomposition energy (top panel) and mixing enthalpy (bottom pane) in $Cs_xFA_{1-x}PbI_3$. Credit adapted from (Dalpian et al., 2019).

(E) A shift in emission energy from their original position depicts how the high-energy peak (E_1) is red-shifting from pure $CsPbI_3$ due to the incorporation of FA^+ and how the low-energy peak (E_2) is blue-shifting from pure $FAPbI_3$ due to incorporation of Cs^+ over time.

(F) Arrhenius plot showing the rates of conversion of $CsPbI_3$ (k_1, bottom panel) and FAPbI3 (k_2, top panel) into $Cs_{1-x}FA_xPbI_3$ against 1/T (T being the absolute temperature). Credit adapted from (Hazarika et al., 2018).

(G) Mixing enthalpy and free energy of mixed I/Br perovskites in the dark. Credit adapted from (Chen et al., 2021).

fewer ion pathways than $MAPb(I_{0.5}Br_{0.5})_3$ perovskites, which raises hurdles to phase segregation. Moreover, adding small amounts of Cs^+ in Br^--I^- mixed composition showed better phase stability than $FAPb(I_xBr_{1-x})_3$ perovskite. Besides, the other A site cations like 2-choloroethylammonium (CIEA), methylenediammonium (MDA) and Imidazole (IZ) can also stabilize the inorganic-organic hybrid perovskites (Kim et al., 2019a, 2020a; Shirzadi et al., 2019). Shirzadi et al. also achieved a PCE over 19% in $MA_{0.95}CIEA_{0.05}PbI_3$ PSCs with superior thermal stability as high as 80°C when introducing 5% CIEA cations (Figure 10C) (Shirzadi et al., 2019).

Pure $FAPbI_3$ has a non-perovskite phase (hexagonal δ-phase, yellow phase) at room temperature. The transition to the perovskite phase (cubic α-phase, black phase) occurs at a higher temperature (433 K), which indicated thermodynamically unstable under an ambient atmosphere(Jeon et al., 2015). Incorporating Br^- with high concentration would anchor the $FAPbI_3$ phase with a thermodynamically favored trend. Compared to I^-, higher activation energy of ion migration for Br^- can be considered to harder and slower transportation within perovskite film. Beal et al. explored the relationship between phase segregation and crystallographic phase behavior by $FA_yCs_{1-y}Pb(Br_xI_{1-x})_3$ alloys (Beal et al., 2020). The phase boundary, deemed to a solvus, indicated mixed cubic-tetragonal phases rather than pure perovskite phase. Seok et al. stabilized the α-$FAPbI_3$ phase by doping $MDACl_2$ to form $FAPbI_3$:0.38$MDACl_2$ perovskites(Min et al., 2019). This approach has been proved that $MDACl_2$ has been successfully incorporated into perovskite lattice to stabilize the α-$FAPbI_3$ phase, which was expected to superior light stability without encapsulation. Similar to $FAPbI_3$, the photo-active black phase of $CsPbI_3$ is unstable at room temperature, while the yellow phase of $CsPbI_3$ is stable due to the low free energy formation. To enhance the phase stability in $CsPbI_3$ PSCs, Nam et al. chose K^+ to stabilize the contraction of $(PbI_6)^{4-}$ octahedral volume (with a perovskite structure of $Cs_{0.925}K_{0.075}PbI_2Br$) and fulfilled improved phase stability (Nam et al., 2017). Guo et al. introduced Rb^+ to partly replace Cs^+ and formed $Cs_{0.99}Rb_{0.01}PbI_2Br$ perovskites (Guo et al., 2019). These optimizations of A sites delivered a high PCE of 12% after 350°C annealing. Moreover, Liu et al. introduced dimethylammonium (DMA^+) and formed an optimized $Cs_{0.5}DMA_{0.5}PbI_3$ PSCs with good stability after 20 days of air exposure (Pei et al., 2019).

Subsequently, Hu et al. established a relationship between grain size and phase segregation in halide hybrid perovskites (Hu et al., 2021). The phase segregation brings in low-bandgap I^--rich domains and large bandgap Br^--rich domains when the average grain size is over 43 nm, which acts as a recombination center to reduce the photovoltaic performance under illumination. Pool et al. applied radiative thermal annealing to replace traditional thermal annealing and proved the similar size of precursor and perovskite phase. Meanwhile, the phase transformation always undergoes three signs of progress: from the precursor phase to the perovskite phase, and then to the perovskite phase-PbI_2 phase. When annealing at 100°C, the $FAPbI_3$ peak showed obvious non-perovskite polymorph (Jeon et al., 2015).

Reduced electron-phonon coupling in mixed perovskites. For photo-stable mixed halide perovskites, high ion conductivity and their electro-mechanical property are identified as key adverse effects to result in I^--rich charge-carrier traps and reduced photovoltaic performance under illumination. Bischak et al. systematically illustrated the extent and dynamics of phase segregation linking to the electron-phonon coupling strength in $Cs_yMA_{1-y}Pb(I_xBr_{1-x})_3$ perovskites (Bischak et al., 2018). The formation and disappearance of I^--rich cluster had been observed both in pure $MAPbI_3$ and $Cs_{0.39}MA_{0.61}Pb(I_{0.15}Br_{0.85})_3$ perovskites at a short light exposure time (<1 min), while this phenomenon continued in pure $MAPbI_3$ perovskites at long light exposure time (around 3 min). Though the photoinduced phase segregation inevitably forms the I^--rich cluster, the stable state can be reached rapidly since the photoinduced carriers can not generate sufficient local strain to stabilize the I^--rich cluster. The $Cs_{0.39}MA_{0.61}Pb(I_{0.15}Br_{0.85})_3$ perovskites exhibited weaker bound and large polaron with smaller accompanying strain field compared to $MAPbI_3$ perovskites, thus reducing the driving force for phase segregation. Notably, the polaronic strain locally alters the free energy of halide hybrid perovskites due to the strong electron-phonon coupling, resulting in stabilized I^--rich cluster(Guzelturk et al., 2018; Ivanovska et al., 2017). Therefore, reducing electron-phonon coupling is a viable method to suppress phase segregation. Diez-Cabanes et al. confirmed that the dominating contribution to the broadening of optical absorption in halide hybrid perovskites stems from the co-existence of varying degrees of segregated phase rather than the configurational disorder (Diez-Cabanes et al., 2021). The phase segregation severely affects the balance of electron/hole transport and collection at the electrodes. The temporal fluctuations of femtosecond laser pulse intensity indicated fewer intensity

fluctuations in mixed perovskite films than $MAPbI_3$ films. Furthermore, Cs^+ ions can alleviate photo-induced phase segregation in virtue of the reduced polarizability (Bischak et al., 2017, 2018). Li et al. boosted a PCE over 21% with $Cs_{0.05}FA_{0.81}MA_{0.14}Pb(I_{0.85}Br_{0.15})_3$ composition with Br^--rich seeding growth strategy (Li et al., 2019). The less appeared PbI_2 peak for Br^--rich perovskite implied excellent thermal stability after 150°C heating. Besides, the hole traps in $MAPbI_3$, which are related to Pb vacancy, undeniably generate after moisture exposure (Qin et al., 2016, 2017). Qin et al. found generated carrier traps in $MAPbI_3$ under 85°C (Qin et al., 2019b).

The relationship between free energy, enthalpy, entropy, and halide segregation. The difference of band gap between I^--rich domains and mixed I^-/Br^--rich domains is the driving force behind the segregation, where photoinduced charge carrier can decrease their free energy by funneling to I^--rich domains (Wang et al., 2019c). Dalpian et al. calculated the linking in the band gap, decomposition energy, and mixing enthalpy in A/X sites alloying (Figure 10D) (Dalpian et al., 2019). The decomposition energy is large for the perovskite formula with organic molecules, where inserting Cs^+ can reduce the decomposition of Pb-based perovskites. Meanwhile, increasing mixing enthalpy is beneficial for removing the distortions, which largely increase the total energy of the perovskite system. Moreover, the change in mixing enthalpy caused by charge transfer is much larger in A site alloying than in B site alloying. Further, Hazarika et al. formed phase-stable $Cs_{1-x}FA_xPbI_3$ perovskites via A site ion exchange (Figures 10E and 10F) (Hazarika et al., 2018). Through fitting the high energy and low energy peak, the activation energy of $Cs_{1-x}FA_xPbI_3$ perovskites is around 0.65 eV, showing a higher value than that for I^- diffusion in MA^+/FA^+-based perovskites (Haruyama et al., 2015). Chen et al. applied a unified theory to understand halide phase segregation in $MAPb(I_{1-x}Br_x)_3$, $CsPb(I_{1-x}Br_x)_3$, $FAPb(I_{1-x}Br_x)_3$, $FA_{7/8}Cs_{1/8}Pb(I_{1-x}Br_x)_3$ and $MA_{7/8}Cs_{1/8}Pb(I_{1-x}Br_x)_3$ perovskites (Figure 10G) (Chen et al., 2021). The calculated width of the distribution in mixing enthalpy for single A site perovskites showed an increasing tendency in the order Cs^+-MA^+-FA^+ of increasing cation size. Due to the large ion size of I^- than Br^-, the $CsPb(I_{1-x}Br_x)_3$ demonstrated the best strain adaptation to the lattice, followed by $MAPb(I_{1-x}Br_x)_3$, and $FAPb(I_{1-x}Br_x)_3$. The mixing free energy curves indicated that the $CsPb(I_{1-x}Br_x)_3$ perovskites had the largest symmetry, while $FAPb(I_{1-x}Br_x)_3$ had the least symmetry. Light-induced halide phase segregation is based on the reduction of free energy of photoinduced charge carriers to nucleated phases with different halide compositions and lower band gap than the parent phase. Barker et al. elucidated that cubic-to-tetragonal phase transition mitigated the phase segregation of $MAPb(I_xBr_{1-x})_3$ alloys, different from the phase boundary in $Cs_xFA_{1-x}Pb(I_yBr_{1-y})_3$ system (Samu et al., 2017). To fulfill the minimum Gibbs free energy, the PL peak of high concentration of Br^- exhibit a short wavelength at the beginning and then red-shifted due to finished phase degradation. Therefore, the phase boundaries in multi-compositions could yield an energetic barrier and reduce phase segregation, together with an increased activation energy of $I^-/Br^-/Cl^-$ migration by decreased symmetry of the tetragonal lattice.

Residual strain control

Tensile strain in perovskite thin films acts as an important source for intrinsic instability to weaken the bonding and favor the defect formation and lower the activation energy for the ion pathway (Li et al., 2021; Wang et al., 2022; Zhao et al., 2017). Thus, strain regulation strategies through compositional alloying could balance the lattice strain. The intrinsic instability of α-$FAPbI_3$ roots in anisotropic and strained lattice along (111), which driving adverse phase transitions from perovskite phase (α-$FAPbI_3$) to non-perovskite phase (δ-$FAPbI_3$) (Zheng et al., 2016). Ye et al. inserted cubic $CsPbBr_3$ interlayer to fulfill the relaxed and high-purity tetragonal phase of $MAPbI_3$ films near the mesoporous TiO_2 region (Ye et al., 2021). Cho et al. also implied that the Cs-doped $(FA_{0.9}MA_{0.1})Pb(I_xBr_{1-x})_3$ perovskites exhibited enhanced light stability over 500 h (Cho et al., 2021). The Cs^+ contributes the release of lattice stress because of the lattice contraction of Br^--introduced composition. Due to the higher formation energy of H-Br and H-Cl bonding than H-I bonding, the mixed halide in X site breaks down the Pb-I bonding in crystal framework and shows robust moisture stability in perovskite alloy (Bodesheim et al., 2020; Svane et al., 2017). Besides, Chen et al. demonstrated that the inhomogeneous residual stress distributed across the vertical direction of perovskite films, wherein the tensile strain remarkably decreased from surface to bottom (Zhu et al., 2019). The inhomogeneous residual strain is contributed to gradient distribution of MA^+ cations (Figures 11A), instead of FA^+, Cs^+, Br^-, or I^-. After flipping over the thin films for $FA_{0.85}MA_{0.15}Cs_{0.05}Pb(I_{0.85}Br_{0.15})_3$ perovskites with annealing processes, the tensile strain inhomogeneity was significantly reduced across the film (Figures 11B). Mao et al. observed that the carrier-induced strain gradient distribution would vanish at high carrier densities, which suppressing photo-induced halide segregation (Mao et al., 2021). The I^- diffusion

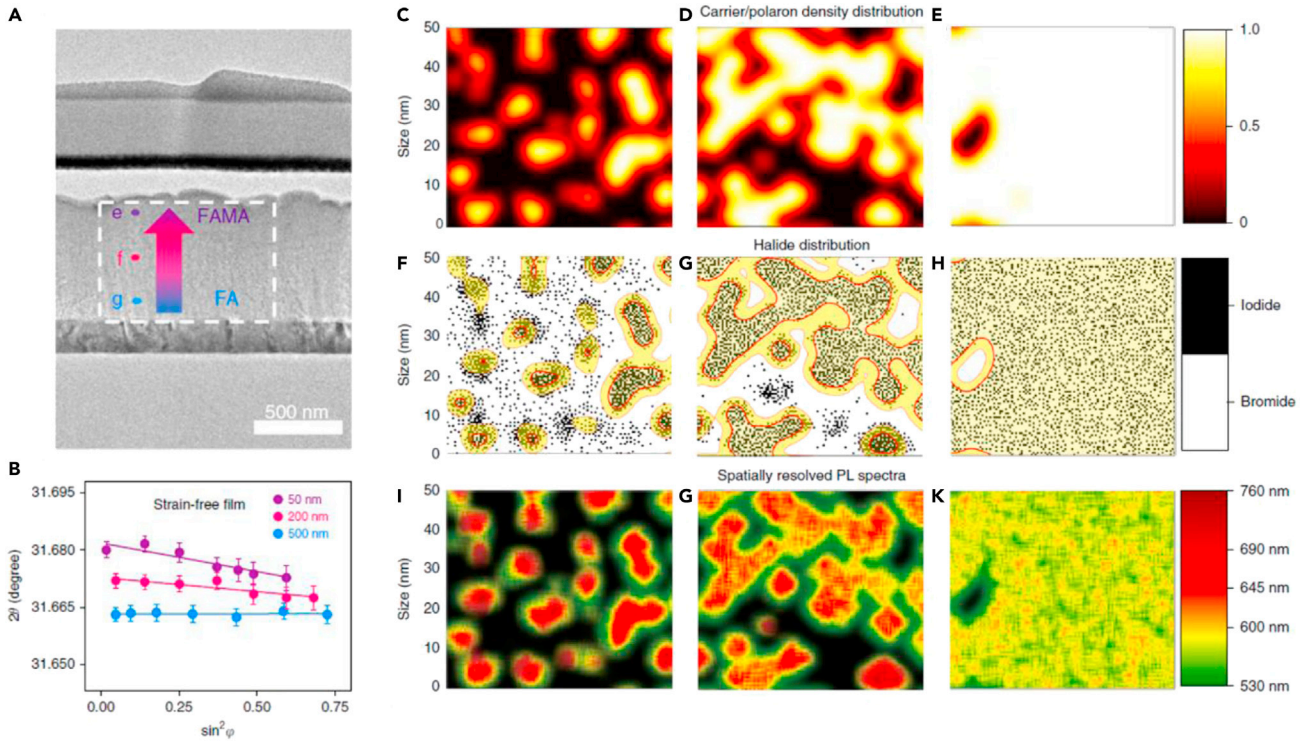

Figure 11. Residual strain in perovskites

(A) The cross-sectional TEM image of the FAMA hybrid perovskite phase.

(B–E) The GIWAXS spectra in the depth of 50, 200, 500 nm for a strain-free film. Credit adapted from (Zhu et al., 2019). The illustration of polaron distribution at (C) low, (D) medium, and (E) high carrier densities.

(F–K) halide distribution and (I-K) spatially resolved PL emission peak wavelengths corresponding to (C), (D), and (E), respectively. Credit adapted from (Mao et al., 2021).

within the area delimiting by polaron can alter halide composition distribution. Interestingly, the polaron value showed an increasing tendency in size, when the photon flux increasing from low to high, and starts to merge until a near continuum occurring (Figures 11C–11E). Correspondingly, I^- segregation occurred at the area with isolated polaron at low and medium photon flux. While the driving force for segregation (e.g., strain gradient) disappeared at high photon flux (Figures 11F–11H), the halide distribution becomes homogeneous across the excited region. The PL spectra in Figures 11I–11K showed phase-segregated I^--rich emission in 620 nm, intermediate wavelength in region where polaron starts to merge, and uniform green emission in ~570 nm, respectively.

Stoichiometric control

For high-performance PSCs, precise precursor stoichiometry is a benefit for industrialization with standardization production. For pure $MAPbI_3$ perovskite films, they have poor moisture stability in the long run. Though the presence of excess A sites is a controversial issue in high-performance PSCs, Haggfeldt et al. found that excess organic halide contributed to low charge carrier mobility and decreased electron injection from the absorber to CTL in n-i-p structure(Jacobsson et al., 2016). Interestingly, the device with excess A sites achieved a record V_{oc}od 1.20 V with high PL intensity, long charge carrier lifetime, and excellent crystal quality. The ion migration and photon-stability also improved in A-site-excess samples.

To obtain long-term device stability in $Cs_{0.05}(MA_{0.17}FA_{0.83})_{0.95}Pb(I_{0.83}Br_{0.17})_3$ perovskites, Hidalgo et al. demonstrated crystallographic reorientation under high moisture exposure with excess organics (Hidalgo et al., 2020). When adding 5% excess A sites, a lower micro-strain and decreased phase segregation were detected by XRD techniques, which indicated a reduced defect in the lattice (Wang et al., 2022). When

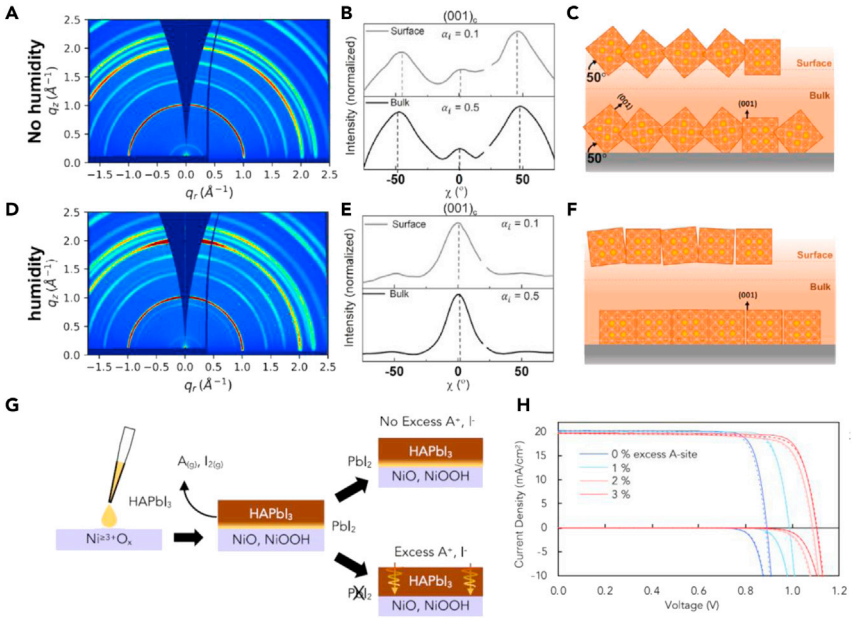

Figure 12. Precursor stoichiometry effect in perovskites

(A–C) GIWAXS, (B) integrated intensity at the incident angle at 0.1° (surface) and 0.50° (bulk), and (C) schematic of crystallographic reorientation at the surface and bulk along (011) plane for excess A sites before exposure to moisture.

(D–F) GIWAXS, (E) integrated intensity at the incident angle at 0.1° (surface) and 0.50° (bulk), and (F) schematic of crystallographic reorientation at the surface and bulk along (011) plane for excess A sites after exposure to moisture. Credit adapted from (Hidalgo et al., 2020).

(G) Schematic of adding excess A sites to precursor perovskites.

(H) J-*V* curves of mixed perovskites with 0–3 mol% excess A sites. Credit adapted from (Boyd et al., 2020).

exposed to moisture, both the surface and bulk perovskite films exhibited crystallographic reorientation in the polycrystalline films (Figures 12A–12F). The (001) plane was oriented along $\chi = 0°$ both the bulk and surface after exposure to moisture, which correlated to structural stability due to well-aligned lattice order. Moreover, excess MAI in mixed perovskite films accordingly slow down the grain growth process during annealing and adjust crystal domains growth. Park et al. added 6 mol% excess MAI and yielded 20.1% efficiency with elevated V_{oc} and FF especially. Recently, McGehee et al. reported over 200 mV enhancement in V_{oc} by blending 1–5 mol% excess A sites in $Cs_{0.25}FA_{0.75}Pb(Br_{0.2}I_{0.8})_3$ and $Cs_{0.05}MA_{0.16}FA_{0.79}Pb_{1.03}(Br_{0.16}I_{0.86})_3$ perovskites precursors in inverted devices (Figures 12G–12H) (Boyd et al., 2020). Excess A sites mitigate electron transfer-proton transfer reactions between precursors and contact electrodes (nickel oxide, NiO_x), which acted as Brønsted and Lewis acid-base reaction (Figure 12G) (Wang et al., 2020b) Therefore, managing the precursor stoichiometry from organic halides may be a performable strategy for both stability and scalability.

SUMMARY AND PERSPECTIVE

PSCs, as an astonishing technology in solar energy harvesting over the past decade, offers high efficiency with simple fabrication. Their remarkable merits include long electron-hole diffusion length, high extinction coefficients and wide absorption range as well as enhanced light/moisture/thermal stability. Here, we first summarized the degradation process under light/moisture/thermal/mechanical stress. Based on the instability issue, we further discussed the A/X sites component regulation from the band gap alignment, charge-carrier dynamics, ion migration and hysteresis, crystallinity and phase control, and stoichiometric control to improve the device stability.

The composition alloying in PSCs affords significant insights to further improvements of PCE and device stability and provides a feasible pathway to fulfill the goals of over 30% efficiency with low-cost and large-area application. The highest record of PCE appears on the mixed perovskite precursor with a structure of $FAPbI_3$:0.38$MDACl_2$ with superior ambient stability (Min et al., 2019, 2021). On the one hand,

the modification of A sites with a mixture of either Cs/FA or Cs/MA/FA represent the easily applied strategy of increasing stability in $APbX_3$ perovskites with a small effect on their band gap. On the other hand, the photovoltaic absorption capacity can be adjusted by multi-X site structure. The X^- mixing in halide perovskites has a crucial role to achieve optimum band gap or tandem device application. Combining A and X sites is a promising channel to decrease defect level and optimize band level alignment. The most common mixed perovskite structure occur on $(FA_{0.85}MA_{0.1}Cs_{0.05})Pb(I_{0.83}Br_{0.17})_3$ (Lee et al., 2015; Singh and Miyasaka, 2018; Hu et al., 2018; Saliba et al., 2016; Hidalgo et al., 2020). This perovskite shows stable photon-stability under charge-extraction conditions. Meanwhile, the following issues should be well considered and addressed.

(i) The perovskites have the characteristics of suitable band-gap, weak exciton binding, high optical absorption, and charge-carrier mobility. Exploring the components engineering requires a systematic strategy to generate unique and superior combinations within a set of variables. The judicious choice of A/X sites promisingly improves the crystallinity and reduces trap densities in perovskite films. Meanwhile, a deeper understanding between physical mechanism and chemical component in A/X sites of perovskite is highly needed.

(ii) The phase stability of perovskite is a key to future large-scale employment. The FA^+/Cs^+-mixed perovskites offer increased phase stability and enhanced strain energy of I^--rich domains, favoring the location of polarons and nucleate. Additionally, blocking the ion migration pathway through triple- or quadruple-cations induction provides an efficient way to suppress anomalous effects such as J-*V* hysteresis and photon-induced phase segregation. Concerning the thermodynamically mechanism, increasing the local energy barriers to repel halogen vacancies could significantly hinder ion migration even under external stress.

(iii) The local lattice strain due to lattice mismatch in ABX_3 structure has a great impact on their physical properties. How to release the tensile strain is a key step to future research. The intrinsic stability of perovskites is still the heart of device performance. Future works should focus on the regulation of intrinsic properties via materials design and component optimization to obtain robust light-absorbing layers, which could benefit the intrinsic shielding and reinforcement for enhanced chemical and mechanical stability.

ACKNOWLEDGMENTS

This work was financially supported by the National Natural Science Foundation of China (51702038), the Science and Technology Department of Sichuan Province (2020YFG0061), and the Recruitment Program for Young Professionals.

DECLARATION OF INTERESTS

The author declares no conflict of interest.

REFERENCES

Abdi-Jalebi, M., Andaji-Garmaroudi, Z., Cacovich, S., Stavrakas, C., Philippe, B., Richter, J.M., Alsari, M., Booker, E.P., Hutter, E.M., Pearson, A.J., et al. (2018). Maximizing and stabilizing luminescence from halide perovskites with potassium passivation. Nature *555*, 497–501.

Akbulatov, A.F., Luchkin, S.Y., Frolova, L.A., Dremova, N.N., Gerasimov, K.L., Zhidkov, I.S., Anokhin, D.V., Kurmaev, E.Z., Stevenson, K.J., and Troshin, P.A. (2017). Probing the intrinsic thermal and photochemical stability of hybrid and inorganic lead halide perovskites. J. Phys. Chem. Lett. *8*, 1211–1218.

Alharbi, E.A., Baumeler, T.P., Krishna, A., Alyamani, A.Y., Eickemeyer, F.T., Ouellette, O., Pan, L., Alghamdi, F.S., Wang, Z., Alotaibi, M.H., et al. (2021). Formation of high-performance multi-cation halide perovskites photovoltaics by δ-$CsPbI_3$/δ-$RbPbI_3$ seed-assisted heterogeneous nucleation. Adv. Energy Mater. *11*, 2003785.

Amat, A., Mosconi, E., Ronca, E., Quarti, C., Umari, P., Nazeeruddin, M.K., Grätzel, M., and De Angelis, F. (2014). Cation-induced band-gap tuning in organohalide perovskites: Interplay of spin–orbit coupling and octahedra tilting. Nano Lett. *14*, 3608–3616.

Aristidou, N., Eames, C., Sanchez-Molina, I., Bu, X., Kosco, J., Islam, M.S., and Haque, S.A. (2017). Fast oxygen diffusion and iodide defects mediate oxygen-induced degradation of perovskite solar cells. Nat. Commun. *8*, 15218.

Bartel, C.J., Sutton, C., Goldsmith, B.R., Ouyang, R., Musgrave, C.B., Ghiringhelli, L.M., and Scheffler, M. (2019). New tolerance factor to predict the stability of perovskite oxides and halides. Sci. Adv. *5*, eaav0693.

Baumann, A., Väth, S., Rieder, P., Heiber, M.C., Tvingstedt, K., and Dyakonov, V. (2015). Identification of trap states in perovskite solar cells. J. Phys. Chem. Lett. *6*, 2350–2354.

Beal, R.E., Hagström, N.Z., Barrier, J., Gold-Parker, A., Prasanna, R., Bush, K.A., Passarello, D., Schelhas, L.T., Brüning, K., Tassone, C.J., et al. (2020). Structural origins of light-induced phase segregation in organic-inorganic halide perovskite photovoltaic materials. Matter *2*, 207–219.

Bi, E., Chen, H., Xie, F., Wu, Y., Chen, W., Su, Y., Islam, A., Gratzel, M., Yang, X., and Han, L. (2017). Diffusion engineering of ions and charge carriers for stable efficient perovskite solar cells. Nat. Commun. *8*, 15330.

Biega, R.-I., Filip, M.R., Leppert, L., and Neaton, J.B. (2021). Chemically localized resonant excitons in silver–pnictogen halide double perovskites. J. Phys. Chem. Lett. *12*, 2057–2063.

Bischak, C.G., Hetherington, C.L., Wu, H., Aloni, S., Ogletree, D.F., Limmer, D.T., and Ginsberg, N.S. (2017). Origin of reversible photoinduced phase separation in hybrid perovskites. Nano Lett. *17*, 1028–1033.

Bischak, C.G., Wong, A.B., Lin, E., Limmer, D.T., Yang, P., and Ginsberg, N.S. (2018). Tunable polaron distortions control the extent of halide demixing in lead halide perovskites. J. Phys. Chem. Lett. *9*, 3998–4005.

Bodesheim, D., Kieslich, G., Johnson, M., and Butler, K.T. (2020). Understanding the balance of entropy and enthalpy in hydrogen–halide noncovalent bonding. J. Phys. Chem. Lett. *11*, 3495–3500.

Boyd, C.C., Shallcross, R.C., Moot, T., Kerner, R., Bertoluzzi, L., Onno, A., Kavadiya, S., Chosy, C., Wolf, E.J., Werner, J., et al. (2020). Overcoming redox reactions at perovskite-nickel oxide interfaces to boost voltages in perovskite solar cells. Joule *4*, 1759–1775.

Boziki, A., Kubicki, D.J., Mishra, A., Meloni, S., Emsley, L., Grätzel, M., and Rothlisberger, U. (2020). Atomistic origins of the limited phase stability of Cs^+-rich $FA_xCs_{(1-x)}PbI_3$ mixtures. Chem. Mater. *32*, 2605–2614.

Brennan, M.C., Draguta, S., Kamat, P.V., and Kuno, M.J.A.E.L. (2017). Light-induced anion phase segregation in mixed halide perovskites. ACS Energy Lett. *3*, 201–213.

Brennan, M.C., Ruth, A., Kamat, P.V., and Kuno, M. (2020). Photoinduced anion segregation in mixed halide perovskites. Trends Chem. *2*, 282–301.

Brivio, F., Walker, A.B., and Walsh, A. (2013). Structural and electronic properties of hybrid perovskites for high-efficiency thin-film photovoltaics from first-principles. APL Mater. *1*, 042111.

Bush, K.A., Frohna, K., Prasanna, R., Beal, R.E., Leijtens, T., Swifter, S.A., and McGehee, M.D. (2018). Compositional engineering for efficient wide band gap perovskites with improved stability to photoinduced phase segregation. ACS Energy Lett. *3*, 428–435.

Chen, B., Yang, M., Zheng, X., Wu, C., Li, W., Yan, Y., Bisquert, J., Garcia-Belmonte, G., Zhu, K., and Priya, S. (2015a). Impact of capacitive effect and ion migration on the hysteretic behavior of perovskite solar cells. J. Phys. Chem. Lett. *6*, 4693–4700.

Chen, Q., Zhou, H., Fang, Y., Stieg, A.Z., Song, T.-B., Wang, H.-H., Xu, X., Liu, Y., Lu, S., You, J., et al. (2015b). The optoelectronic role of chlorine in $CH_3NH_3PbI_3$(Cl)-based perovskite solar cells. Nat. Commun. *6*, 7269.

Chen, T., Foley, B.J., Ipek, B., Tyagi, M., Copley, J.R.D., Brown, C.M., Choi, J.J., and Lee, S.-H. (2015c). Rotational dynamics of organic cations in the $CH_3NH_3PbI_3$ perovskite. Phys. Chem. Chem. Phys. *17*, 31278–31286.

Chen, T., Foley, B.J., Park, C., Brown, C.M., Harriger, L.W., Lee, J., Ruff, J., Yoon, M., Choi, J.J., and Lee, S.-H. (2016). Entropy-driven structural transition and kinetic trapping in formamidinium lead iodide perovskite. Sci. Adv. *2*, e1601650.

Chen, Y., Tan, S., Li, N., Huang, B., Niu, X., Li, L., Sun, M., Zhang, Y., Zhang, X., Zhu, C., et al. (2020). Self-elimination of intrinsic defects improves the low-temperature performance of perovskite photovoltaics. Joule *4*, 1961–1976.

Chen, L., Tan, Y.-Y., Chen, Z.-X., Wang, T., Hu, S., Nan, Z.-A., Xie, L.-Q., Hui, Y., Huang, J.-X., Zhan, C., et al. (2019a). Toward long-term stability: single-crystal alloys of cesium-containing mixed cation and mixed halide perovskite. J. Am. Chem. Soc. *141*, 1665–1671.

Chen, Y., Yang, Z., Jia, X., Wu, Y., Yuan, N., Ding, J., Zhang, W.-H., and Liu, S. (2019b). Thermally stable methylammonium-free inverted perovskite solar cells with Zn^{2+} doped $CuGaO_2$ as efficient mesoporous hole-transporting layer. Nano Energy *61*, 148–157.

Chen, Z., Brocks, G., Tao, S., and Bobbert, P.A. (2021). Unified theory for light-induced halide segregation in mixed halide perovskites. Nat. Commun. *12*, 2687.

Cheng, Z., and Lin, J. (2010). Layered organic–inorganic hybrid perovskites: Structure, optical properties, film preparation, patterning and templating engineering. CrystEngComm. *12*, 2646–2662.

Cho, S.H., Byeon, J., Jeong, K., Hwang, J., Lee, H., Jang, J., Lee, J., Kim, T., Kim, K., Choi, M., and Lee, Y.S. (2021). Investigation of defect-tolerant perovskite solar cells with long-term stability via controlling the self-doping effect. Adv. Energy Mater. *11*, 2100555.

Cho, Y., Soufiani, A.M., Yun, J.S., Kim, J., Lee, D.S., Seidel, J., Deng, X., Green, M.A., Huang, S., and Ho-Baillie, A.W.Y. (2018). Mixed 3D–2D passivation treatment for mixed-cation lead mixed-halide perovskite solar cells for higher efficiency and better stability. Adv. Energy Mater. *8*, 1703392.

Correa-Baena, J.P., Luo, Y.Q., Brenner, T.M., Snaider, J., Sun, S.J., Li, X.Y., Jensen, M.A., Hartono, N.T.P., Nienhaus, L., Wieghold, S., et al. (2019). Homogenized halides and alkali cation segregation in alloyed organic-inorganic perovskites. Science *363*, 627–631.

Cortecchia, D., Dewi, H.A., Yin, J., Bruno, A., Chen, S., Baikie, T., Boix, P.P., Grätzel, M., Mhaisalkar, S., Soci, C., and Mathews, N. (2016). Lead-free $MA_2CuCl_xBr_{4-x}$ hybrid perovskites. Inorg. Chem. *55*, 1044–1052.

Dalpian, G.M., Zhao, X.-G., Kazmerski, L., and Zunger, A. (2019). Formation and composition-dependent properties of alloys of cubic halide perovskites. Chem. Mater. *31*, 2497–2506.

Dang, H.X., Wang, K., Ghasemi, M., Tang, M.-C., De Bastiani, M., Aydin, E., Dauzon, E., Barrit, D., Peng, J., Smilgies, D.-M., et al. (2019). Multi-cation synergy suppresses phase segregation in mixed-halide perovskites. Joule *3*, 1746–1764.

Deepa, M., Salado, M., Calio, L., Kazim, S., Shivaprasad, S.M., and Ahmad, S. (2017). Cesium power: Low Cs+ levels impart stability to perovskite solar cells. Phys. Chem. Chem. Phys. *19*, 4069–4077.

Deng, Y., Xu, S., Chen, S., Xiao, X., Zhao, J., and Huang, J. (2021). Defect compensation in formamidinium–caesium perovskites for highly efficient solar mini-modules with improved photostability. Nat. Energy *6*, 633–641.

deQuilettes, D.W., Zhang, W., Burlakov, V.M., Graham, D.J., Leijtens, T., Osherov, A., Bulović, V., Snaith, H.J., Ginger, D.S., and Stranks, S.D. (2016). Photo-induced halide redistribution in organic–inorganic perovskite films. Nat. Commun. *7*, 11683.

Diez-Cabanes, V., Even, J., Beljonne, D., and Quarti, C. (2021). Electronic structure and optical properties of mixed iodine/bromine lead perovskites. to mix or not to mix? Adv. Opt. Mater. https://doi.org/10.1002/adom.202001832.

Domanski, K., Roose, B., Matsui, T., Saliba, M., Turren-Cruz, S.-H., Correa-Baena, J.-P., Carmona, C.R., Richardson, G., Foster, J.M., De Angelis, F., et al. (2017). Migration of cations induces reversible performance losses over day/night cycling in perovskite solar cells. Energy Environ. Sci. *10*, 604–613.

Dong, Q., Zhu, C., Chen, M., Jiang, C., Guo, J., Feng, Y., Dai, Z., Yadavalli, S.K., Hu, M., Cao, X., et al. (2021). Interpenetrating interfaces for efficient perovskite solar cells with high operational stability and mechanical robustness. Nat. Commun. *12*, 973.

Eames, C., Frost, J.M., Barnes, P.R.F., O'Regan, B.C., Walsh, A., and Islam, M.S. (2015). Ionic transport in hybrid lead iodide perovskite solar cells. Nat. Commun. *6*, 7497.

Eperon, G.E., Stranks, S.D., Menelaou, C., Johnston, M.B., Herz, L.M., and Snaith, H.J. (2014). Formamidinium lead trihalide: A broadly tunable perovskite for efficient planar heterojunction solar cells. Energy Environ. Sci. *7*, 982–988.

Faghihnasiri, M., Izadifard, M., and Ghazi, M.E. (2017). DFT study of mechanical properties and stability of cubic methylammonium lead halide perovskites ($CH_3NH_3PbX_3$, X = I, Br, Cl). J. Phys. Chem. C *121*, 27059–27070.

Fang, Z., Zeng, Q., Zuo, C., Zhang, L., Xiao, H., Cheng, M., Hao, F., Bao, Q., Zhang, L., Yuan, Y., et al. (2021). Perovskite-based tandem solar cells. Sci. Bull. *66*, 621–636.

Fedeli, P., Gazza, F., Calestani, D., Ferro, P., Besagni, T., Zappettini, A., Calestani, G., Marchi, E., Ceroni, P., and Mosca, R. (2015). Influence of the synthetic procedures on the structural and optical properties of mixed-halide (Br, I) perovskite films. J. Phys. Chem. C *119*, 21304–21313.

Ferdani, D.W., Pering, S.R., Ghosh, D., Kubiak, P., Walker, A.B., Lewis, S.E., Johnson, A.L., Baker, P.J., Islam, M.S., and Cameron, P.J. (2019). Partial cation substitution reduces iodide ion transport in lead iodide perovskite solar cells. Energy Environ. Sci. *12*, 2264–2272.

Frost, J.M., Butler, K.T., Brivio, F., Hendon, C.H., van Schilfgaarde, M., and Walsh, A. (2014). Atomistic origins of high-performance in hybrid halide perovskite solar cells. Nano Lett. *14*, 2584–2590.

García-Fernández, A., Juarez-Perez, E.J., Castro-García, S., Sánchez-Andújar, M., Ono, L.K., Jiang, Y., and Qi, Y. (2018). Benchmarking chemical stability of arbitrarily mixed 3D hybrid halide

perovskites for solar cell applications. Small Methods *2*, 1800242.

Ghosh, D., Smith, A.R., Walker, A.B., and Islam, M.S. (2018). Mixed A-cation perovskites for solar cells: Atomic-scale insights into structural distortion, hydrogen bonding, and electronic properties. Chem. Mater. *30*, 5194–5204.

Ghosh, D., Walsh Atkins, P., Islam, M.S., Walker, A.B., and Eames, C. (2017). Good vibrations: Locking of octahedral tilting in mixed-cation iodide perovskites for solar cells. ACS Energy Lett. *2*, 2424–2429.

Grånäs, O., Vinichenko, D., and Kaxiras, E. (2016). Establishing the limits of efficiency of perovskite solar cells from first principles modeling. Sci. Rep. *6*, 36108.

Guo, Y., Zhao, F., Tao, J., Jiang, J., Zhang, J., Yang, J., Hu, Z., and Chu, J. (2019). Efficient and hole-transporting-layer-free $CsPbI_2Br$ planar heterojunction perovskite solar cells through rubidium passivation. ChemSusChem *12*, 983–989.

Guzelturk, B., Belisle, R.A., Smith, M.D., Bruening, K., Prasanna, R., Yuan, Y., Gopalan, V., Tassone, C.J., Karunadasa, H.I., McGehee, M.D., and Lindenberg, A.M. (2018). Terahertz emission from hybrid perovskites driven by ultrafast charge separation and strong electron–phonon coupling. Adv. Mater. *30*, 1704737.

Hao, F., Stoumpos, C.C., Cao, D.H., Chang, R.P.H., and Kanatzidis, M.G. (2014). Lead-free solid-state organic–inorganic halide perovskite solar cells. Nat. Photon. *8*, 489–494.

Hao, M., Bai, Y., Zeiske, S., Ren, L., Liu, J., Yuan, Y., Zarrabi, N., Cheng, N., Ghasemi, M., Chen, P., et al. (2020). Ligand-assisted cation-exchange engineering for high-efficiency colloidal $Cs_{1-x}FA_xPbI_3$ quantum dot solar cells with reduced phase segregation. Nat. Energy *5*, 79–88.

Haruyama, J., Sodeyama, K., Han, L., and Tateyama, Y. (2015). First-principles study of ion diffusion in perovskite solar cell sensitizers. J. Am. Chem. Soc. *137*, 10048–10051.

Hazarika, A., Zhao, Q., Gaulding, E.A., Christians, J.A., Dou, B., Marshall, A.R., Moot, T., Berry, J.J., Johnson, J.C., and Luther, J.M. (2018). Perovskite quantum dot photovoltaic materials beyond the reach of thin films: Full-range tuning of a-site cation composition. ACS Nano *12*, 10327–10337.

He, Y., Wang, S.Q., Xue, X.X., Zhang, L., Chen, K., Zhou, W.X., and Feng, Y. (2018). Ab initio study of the moisture stability of lead iodine perovskites. J. Phys. Condens. Matter *30*, 355501.

Heo, S., Seo, G., Lee, Y., Lee, D., Seol, M., Lee, J., Park, J.-B., Kim, K., Yun, D.-J., Kim, Y.S., et al. (2017). Deep level trapped defect analysis in $CH_3NH_3PbI_3$ perovskite solar cells by deep level transient spectroscopy. Energy Environ. Sci. *10*, 1128–1133.

Heo, S., Seo, G., Lee, Y., Seol, M., Kim, S.H., Yun, D.J., Kim, Y., Kim, K., Lee, J., Lee, J., et al. (2019). Origins of high performance and degradation in the mixed perovskite solar cells. Adv. Mater. *31*, e1805438.

Hidalgo, J., Perini, C.A.R., Castro-Mendez, A.-F., Jones, D., Köbler, H., Lai, B., Li, R., Sun, S., Abate, A., and Correa-Baena, J.-P. (2020). Moisture-induced crystallographic reorientations and effects on charge carrier extraction in metal halide perovskite solar cells. ACS Energy Lett. *5*, 3526–3534.

Hoke, E.T., Slotcavage, D.J., Dohner, E.R., Bowring, A.R., Karunadasa, H.I., and McGehee, M.D. (2015). Reversible photo-induced trap formation in mixed-halide hybrid perovskites for photovoltaics. Chem. Sci. *6*, 613–617.

Hong, Q.-M., Xu, R.-P., Jin, T.-Y., Tang, J.-X., and Li, Y.-Q. (2019). Unraveling the light-induced degradation mechanism of $CH_3NH_3PbI_3$ perovskite films. Org. Electron. *67*, 19–25.

Hu, L., Guan, X., Chen, W., Yao, Y., Wan, T., Lin, C.-H., Pham, N.D., Yuan, L., Geng, X., Wang, F., et al. (2021). Linking phase segregation and photovoltaic performance of mixed-halide perovskite films through grain size engineering. ACS Energy Lett. *6*, 1649–1658.

Hu, Q., Chen, W., Yang, W., Li, Y., Zhou, Y., Larson, B.W., Johnson, J.C., Lu, Y.-H., Zhong, W., Xu, J., et al. (2020). Improving efficiency and stability of perovskite solar cells enabled by a near-infrared-absorbing moisture barrier. Joule *4*, 1575–1593.

Hu, Y., Hutter, E.M., Rieder, P., Grill, I., Hanisch, J., Aygüler, M.F., Hufnagel, A.G., Handloser, M., Bein, T., Hartschuh, A., et al. (2018). Understanding the role of cesium and rubidium additives in perovskite solar cells: Trap states, charge transport, and recombination. Adv. Energy Mater. *8*, 1703057.

Hui, W., Chao, L., Lu, H., Xia, F., Wei, Q., Su, Z., Niu, T., Tao, L., Du, B., Li, D., et al. (2021). Stabilizing black-phase formamidinium perovskite formation at room temperature and high humidity. Science *371*, 1359–1364.

Ippili, S., Jella, V., Kim, J., Hong, S., and Yoon, S.-G. (2018). Enhanced piezoelectric output performance via control of dielectrics in Fe^{2+}-incorporated $MAPbI_3$ perovskite thin films: Flexible piezoelectric generators. Nano Energy *49*, 247–256.

Ivanovska, T., Dionigi, C., Mosconi, E., De Angelis, F., Liscio, F., Morandi, V., and Ruani, G. (2017). Long-lived photoinduced polarons in organohalide perovskites. J. Phys. Chem. Lett. *8*, 3081–3086.

Jacobsson, T.J., Correa-Baena, J.-P., Halvani Anaraki, E., Philippe, B., Stranks, S.D., Bouduban, M.E.F., Tress, W., Schenk, K., Teuscher, J., Moser, J.-E., et al. (2016). Unreacted PbI_2 as a double-edged sword for enhancing the performance of perovskite solar cells. J. Am. Chem. Soc. *138*, 10331–10343.

Jeon, N.J., Noh, J.H., Yang, W.S., Kim, Y.C., Ryu, S., Seo, J., and Seok, S.I. (2015). Compositional engineering of perovskite materials for high-performance solar cells. Nature *517*, 476–480.

Jeong, J., Kim, M., Seo, J., Lu, H., Ahlawat, P., Mishra, A., Yang, Y., Hope, M.A., Eickemeyer, F.T., Kim, M., et al. (2021). Pseudo-halide anion engineering for α-$FAPbI_3$ perovskite solar cells. Nature *592*, 381–385.

Jeong, M., Choi, I.W., Go, E.M., Cho, Y., Kim, M., Lee, B., Jeong, S., Jo, Y., Choi, H.W., Lee, J., et al. (2020). Stable perovskite solar cells with efficiency exceeding 24.8% and 0.3-V voltage loss. Science *369*, 1615–1620.

Jesper Jacobsson, T., Correa-Baena, J.-P., Pazoki, M., Saliba, M., Schenk, K., Grätzel, M., and Hagfeldt, A. (2016). Exploration of the compositional space for mixed lead halogen perovskites for high efficiency solar cells. Energy Environ. Sci. *9*, 1706–1724.

Ji, L.-J., Sun, S.-J., Qin, Y., Li, K., and Li, W. (2019). Mechanical properties of hybrid organic-inorganic perovskites. Coord. Chem. Rev. *391*, 15–29.

Jiang, Y., He, X., Liu, T., Zhao, N., Qin, M., Liu, J., Jiang, F., Qin, F., Sun, L., Lu, X., et al. (2019). Intralayer A-site compositional engineering of ruddlesden–popper perovskites for thermostable and efficient solar cells. ACS Energy Lett. *4*, 1216–1224.

Jin, H., Debroye, E., Keshavarz, M., Scheblykin, I.G., Roeffaers, M.B.J., Hofkens, J., and Steele, J.A. (2020a). It's a trap! on the nature of localised states and charge trapping in lead halide perovskites. Mater.Horiz. *7*, 397–410.

Jin, Z., Zhang, Z., Xiu, J., Song, H., Gatti, T., and He, Z. (2020b). A critical review on bismuth and antimony halide based perovskites and their derivatives for photovoltaic applications: Recent advances and challenges. J. Mater. Chem. A *8*, 16166–16188.

Johnston, A., Walters, G., Saidaminov, M.I., Huang, Z., Bertens, K., Jalarvo, N., and Sargent, E.H. (2020). Bromine incorporation and suppressed cation rotation in mixed-halide perovskites. ACS Nano *14*, 15107–15118.

Juarez-Perez, E.J., Hawash, Z., Raga, S.R., Ono, L.K., and Qi, Y. (2016). Thermal degradation of $CH_3NH_3PbI_3$ perovskite into NH_3 and CH_3I gases observed by coupled thermogravimetry–mass spectrometry analysis. Energy Environ. Sci. *9*, 3406–3410.

Jung, E., Budzinauskas, K., Öz, S., Ünlü, F., Kuhn, H., Wagner, J., Grabowski, D., Klingebiel, B., Cherasse, M., Dong, J., et al. (2020). Femto- to microsecond dynamics of excited electrons in a quadruple cation perovskite. ACS Energy Lett *5*, 785–792.

Jung, E.H., Jeon, N.J., Park, E.Y., Moon, C.S., Shin, T.J., Yang, T.-Y., Noh, J.H., and Seo, J. (2019). Efficient, stable and scalable perovskite solar cells using poly(3-hexylthiophene). Nature *567*, 511–515.

Kamat, P.V., and Kuno, M. (2021). Halide ion migration in perovskite nanocrystals and nanostructures. Acc. Chem. Res. *54*, 520–531.

Kepenekian, M., Robles, R., Katan, C., Sapori, D., Pedesseau, L., and Even, J. (2015). Rashba and dresselhaus effects in hybrid organic–inorganic perovskites: From basics to devices. ACS Nano *9*, 11557–11567.

Kim, H.-S., and Hagfeldt, A. (2019). Photoinduced lattice symmetry enhancement in mixed hybrid perovskites and its beneficial effect on the recombination behavior. Adv. Opt. Mater. *7*, 1801512.

Kim, J., Hwang, T., Lee, B., Lee, S., Park, K., Park, H.H., and Park, B. (2019a). An aromatic diamine molecule as the a-site solute for highly durable and efficient perovskite solar cells. Small Methods *3*, 1800361.

Kim, M., Kim, G.-H., Lee, T.K., Choi, I.W., Choi, H.W., Jo, Y., Yoon, Y.J., Kim, J.W., Lee, J., Huh, D., et al. (2019b). Methylammonium chloride induces intermediate phase stabilization for efficient perovskite solar cells. Joule *3*, 2179–2192.

Kim, G., Min, H., Lee, K.S., Lee, D.Y., Yoon, S.M., and Seok, S.I. (2020a). Impact of strain relaxation on performance of α-formamidinium lead iodide perovskite solar cells. Science *370*, 108–112.

Kim, S., Eom, T., Ha, Y.-S., Hong, K.-H., and Kim, H. (2020b). Thermodynamics of multicomponent perovskites: A guide to highly efficient and stable solar cell materials. Chem. Mater. *32*, 4265–4272.

Kirchartz, T., and Rau, U. (2017). Decreasing radiative recombination coefficients via an indirect band gap in lead halide perovskites. J. Phys. Chem. Lett. *8*, 1265–1271.

Knight, A.J., Borchert, J., Oliver, R.D.J., Patel, J.B., Radaelli, P.G., Snaith, H.J., Johnston, M.B., and Herz, L.M. (2021). Halide segregation in mixed-halide perovskites: Influence of A-site cations. ACS Energy Lett. *6*, 799–808.

Knight, A.J., Patel, J.B., Snaith, H.J., Johnston, M.B., and Herz, L.M. (2020). Trap states, electric fields, and phase segregation in mixed-halide perovskite photovoltaic devices. Adv. Energy Mater. *10*, 1903488.

Koocher, N.Z., Saldana-Greco, D., Wang, F., Liu, S., and Rappe, A.M. (2015). Polarization dependence of water adsorption to $CH_3NH_3PbI_3$ (001) surfaces. J. Phys. Chem. Lett. *6*, 4371–4378.

Krishnamoorthy, T., Ding, H., Yan, C., Leong, W.L., Baikie, T., Zhang, Z., Sherburne, M., Li, S., Asta, M., Mathews, N., and Mhaisalkar, S.G. (2015). Lead-free germanium iodide perovskite materials for photovoltaic applications. J. Mater. Chem. A *3*, 23829–23832.

Kubicki, D.J., Prochowicz, D., Hofstetter, A., Zakeeruddin, S.M., Grätzel, M., and Emsley, L. (2017). Phase segregation in Cs-, Rb- and K-doped mixed-cation (MA)x(FA)1–xPbI3 hybrid perovskites from solid-state NMR. J. Am. Chem. Soc. *139*, 14173–14180.

Lee, J.-H., Deng, Z., Bristowe, N.C., Bristowe, P.D., and Cheetham, A.K. (2018). The competition between mechanical stability and charge carrier mobility in MA-based hybrid perovskites: Insight from DFT. J. Mater. Chem. C *6*, 12252–12259.

Lee, J.-W., Kim, D.-H., Kim, H.-S., Seo, S.-W., Cho, S.M., and Park, N.-G. (2015). Formamidinium and cesium hybridization for photo- and moisture-stable perovskite solar cell. Adv. Energy Mater. *5*, 1501310.

Lee, J.H., Lee, J.-H., Kong, E.-H., and Jang, H.M. (2016). The nature of hydrogen-bonding interaction in the prototypic hybrid halide perovskite, tetragonal $CH_3NH_3PbI_3$. Sci. Rep. *6*, 21687.

Leguy, A.M.A., Frost, J.M., McMahon, A.P., Sakai, V.G., Kockelmann, W., Law, C., Li, X., Foglia, F., Walsh, A., O'Regan, B.C., et al. (2015a). The dynamics of methylammonium ions in hybrid organic–inorganic perovskite solar cells. Nat. Commun. *6*, 7124.

Leguy, A.M.A., Hu, Y., Campoy-Quiles, M., Alonso, M.I., Weber, O.J., Azarhoosh, P., van Schilfgaarde, M., Weller, M.T., Bein, T., Nelson, J., et al. (2015b). Reversible hydration of $CH_3NH_3PbI_3$ in films, single crystals, and solar cells. Chem. Mater. *27*, 3397–3407.

Levine, I., Vera, O.G., Kulbak, M., Ceratti, D.-R., Rehermann, C., Márquez, J.A., Levcenko, S., Unold, T., Hodes, G., Balberg, I., et al. (2019). Deep defect states in wide-band-gap ABX_3 halide perovskites. ACS Energy Lett *4*, 1150–1157.

Li, C., Hu, J., Wang, S., Ren, J., Chen, B., Pan, T., Niu, X., and Hao, F. (2021). Lattice strain relaxation and grain homogenization for efficient inverted $MAPbI_3$ perovskite solar cells. J. Phys. Chem. Lett. *12*, 4569–4575.

Li, C., Wang, A., Deng, X., Wang, S., Yuan, Y., Ding, L., and Hao, F. (2020). Insights into ultrafast carrier dynamics in perovskite thin films and solar cells. ACS Photon. *7*, 1893–1907.

Li, L., Liu, N., Xu, Z., Chen, Q., Wang, X., and Zhou, H. (2017). Precise composition tailoring of mixed-cation hybrid perovskites for efficient solar cells by mixture design methods. ACS Nano *11*, 8804–8813.

Li, Q., Zhao, Y., Zhou, W., Han, Z., Fu, R., Lin, F., Yu, D., and Zhao, Q. (2019). Halogen engineering for operationally stable perovskite solar cells via sequential deposition. Adv. Energy Mater. *9*, 1902239.

Li, Z., Yang, M., Park, J.-S., Wei, S.-H., Berry, J.J., and Zhu, K. (2016). Stabilizing perovskite structures by tuning tolerance factor: Formation of formamidinium and cesium lead iodide solid-state alloys. Chem. Mater. *28*, 284–292.

Liang, C., Gu, H., Xia, Y., Wang, Z., Liu, X., Xia, J., Zuo, S., Hu, Y., Gao, X., Hui, W., et al. (2021). Two-dimensional Ruddlesden–Popper layered perovskite solar cells based on phase-pure thin films. Nat. Energy *6*, 38–45.

Lin, D., Shi, T., Xie, H., Wan, F., Ren, X., Liu, K., Zhao, Y., Ke, L., Lin, Y., Gao, Y., et al. (2021). Ion migration accelerated reaction between oxygen and metal halide perovskites in light and its suppression by cesium incorporation. Adv. Energy Mater. *11*, 2002552.

Liu, Z., Chang, J., Lin, Z., Zhou, L., Yang, Z., Chen, D., Zhang, C., Liu, S., and Hao, Y. (2018). High-performance planar perovskite solar cells using low temperature, solution–combustion-based nickel oxide hole transporting layer with efficiency exceeding 20%. Adv. Energy Mater. *8*, 1703432.

Liu, Z., Krückemeier, L., Krogmeier, B., Klingebiel, B., Márquez, J.A., Levcenko, S., Öz, S., Mathur, S., Rau, U., Unold, T., and Kirchartz, T. (2019). Open-circuit voltages exceeding 1.26 V in planar methylammonium lead iodide perovskite solar cells. ACS Energy Lett. *4*, 110–117.

Longo, G., Mahesh, S., Buizza, L.R.V., Wright, A.D., Ramadan, A.J., Abdi-Jalebi, M., Nayak, P.K., Herz, L.M., and Snaith, H.J. (2020). Understanding the performance-limiting factors of $Cs_2AgBiBr_6$ double-perovskite solar cells. ACS Energy Lett. *5*, 2200–2207.

Lyu, M., Lee, D.-K., and Park, N.-G. (2020). Effect of alkaline earth metal chloride additives BCl_2 (B = Mg, Ca, Sr and Ba) on the photovoltaic performance of $FAPbI_3$ based perovskite solar cells. Nanoscale Horiz *5*, 1332–1343.

Ma, L., Li, W., Yang, K., Bi, J., Feng, J., Zhang, J., Yan, Z., Zhou, X., Liu, C., Ji, Y., et al. (2021). A- or X-site mixture on mechanical properties of $APbX_3$ perovskite single crystals. APL Mater. *9*, 041112.

Mahesh, S., Ball, J.M., Oliver, R.D.J., McMeekin, D.P., Nayak, P.K., Johnston, M.B., and Snaith, H.J. (2020). Revealing the origin of voltage loss in mixed-halide perovskite solar cells. Energy Environ. Sci. *13*, 258–267.

Mao, W., Hall, C.R., Bernardi, S., Cheng, Y.B., Widmer-Cooper, A., Smith, T.A., and Bach, U. (2021). Light-induced reversal of ion segregation in mixed-halide perovskites. Nat. Mater. *20*, 55–61.

Matsui, T., Yamamoto, T., Nishihara, T., Morisawa, R., Yokoyama, T., Sekiguchi, T., and Negami, T. (2019). Compositional engineering for thermally stable, highly efficient perovskite solar cells exceeding 20% power conversion efficiency with 85 °C/85% 1000 h stability. Adv. Mater. *31*, 1806823.

Matsui, T., Yokoyama, T., Negami, T., Sekiguchi, T., Saliba, M., Grätzel, M., and Segawa, H. (2018). Effect of rubidium for thermal stability of triple-cation perovskite solar cells. Chem. Lett. *47*, 814–816.

Meggiolaro, D., Mosconi, E., and De Angelis, F. (2018). Modeling the interaction of molecular iodine with $mapbi_3$: A probe of lead-halide perovskites defect chemistry. ACS Energy Lett *3*, 447–451.

Merdasa, A., Kiligaridis, A., Rehermann, C., Abdi-Jalebi, M., Stöber, J., Louis, B., Gerhard, M., Stranks, S.D., Unger, E.L., and Scheblykin, I.G. (2019). Impact of excess lead iodide on the recombination kinetics in metal halide perovskites. ACS Energy Lett. *4*, 1370–1378.

Merten, L., Hinderhofer, A., Baumeler, T., Arora, N., Hagenlocher, J., Zakeeruddin, S.M., Dar, M.I., Grätzel, M., and Schreiber, F. (2021). Quantifying stabilized phase purity in formamidinium-based multiple-cation hybrid perovskites. Chem. Mater. *33*, 2769–2776.

Min, H., Kim, M., Lee, S.-U., Kim, H., Kim, G., Choi, K., Lee, J.H., and Seok, S.I. (2019). Efficient, stable solar cells by using inherent bandgap of α-phase formamidinium lead iodide. Science *366*, 749–753.

Min, H., Lee, D.Y., Kim, J., Kim, G., Lee, K.S., Kim, J., Paik, M.J., Kim, Y.K., Kim, K.S., Kim, M.G., et al. (2021). Perovskite solar cells with atomically coherent interlayers on SnO_2 electrodes. Nature *598*, 444–450.

Minda, I., Horn, J., Ahmed, E., Schlettwein, D., and Schwoerer, H. (2018). Ultrafast charge dynamics in mixed cation–mixed halide perovskite thin films. ChemPhysChem. *19*, 3010–3017.

Mosconi, E., and De Angelis, F. (2016). Mobile ions in organohalide perovskites: interplay of electronic structure and dynamics. ACS Energy Lett. *1*, 182–188.

Nagabhushana, G.P., Shivaramaiah, R., and Navrotsky, A. (2016). Direct calorimetric verification of thermodynamic instability of lead halide hybrid perovskites. Proc. Natl. Acad. Sci. U.S.A *113*, 7717–7721.

Nam, J.K., Chai, S.U., Cha, W., Choi, Y.J., Kim, W., Jung, M.S., Kwon, J., Kim, D., and Park, J.H. (2017). Potassium incorporation for enhanced performance and stability of fully inorganic cesium lead halide perovskite solar cells. Nano Lett. *17*, 2028–2033.

Nickel, N.H., Lang, F., Brus, V.V., Shargaieva, O., and Rappich, J. (2017). Unraveling the light-induced degradation mechanisms of $CH_3NH_3PbI_3$ perovskite films. Adv. Electron. Mater. *3*, 1700158.

Niu, G., Guo, X., and Wang, L. (2015). Review of recent progress in chemical stability of perovskite solar cells. J. Mater. Chem. A *3*, 8970–8980.

Oranskaia, A., Yin, J., Bakr, O.M., Brédas, J.-L., and Mohammed, O.F. (2018). Halogen migration in hybrid perovskites: The organic cation matters. J. Phys. Chem. Lett. *9*, 5474–5480.

Ouyang, Y., Li, Y., Zhu, P., Li, Q., Gao, Y., Tong, J., Shi, L., Zhou, Q., Ling, C., Chen, Q., et al. (2019). Photo-oxidative degradation of methylammonium lead iodide perovskite: Mechanism and protection. J. Mater. Chem. A *7*, 2275–2282.

Park, B.-w., Zhang, X., Johansson, E.M.J., Hagfeldt, A., Boschloo, G., Seok, S.I., and Edvinsson, T. (2017). Analysis of crystalline phases and integration modelling of charge quenching yields in hybrid lead halide perovskite solar cell materials. Nano Energy *40*, 596–606.

Patil, J.V., Mali, S.S., and Hong, C.K. (2020). A-site rubidium cation-incorporated $CsPbI_2Br$ all-inorganic perovskite solar cells exceeding 17% efficiency. Solar RRL *4*, 2000164.

Pei, Y., Liu, Y., Li, F., Bai, S., Jian, X., and Liu, M. (2019). Unveiling property of hydrolysis-derived $DMAPbI_3$ for perovskite devices: Composition engineering, defect mitigation, and stability optimization. iScience *15*, 165–172.

Qin, C., Matsushima, T., Fujihara, T., and Adachi, C. (2017). Multifunctional benzoquinone additive for efficient and stable planar perovskite solar cells. Adv. Mater. *29*, 1603808.

Qin, C., Matsushima, T., Fujihara, T., Potscavage, W.J., Jr., and Adachi, C. (2016). Degradation mechanisms of solution-processed planar perovskite solar cells: thermally stimulated current measurement for analysis of carrier traps. Adv. Mater. *28*, 466–471.

Qin, C., Matsushima, T., Klotz, D., Fujihara, T., and Adachi, C. (2019a). Device stability: The relation of phase-transition effects and thermal stability of planar perovskite solar cells. Adv. Sci. *6*, 1970004.

Qin, C., Matsushima, T., Klotz, D., Fujihara, T., and Adachi, C. (2019b). The relation of phase-transition effects and thermal stability of planar perovskite solar cells. Adv. Sci. *6*, 1801079.

Quilettes, D.W.d., Vorpahl, S.M., Stranks, S.D., Nagaoka, H., Eperon, G.E., Ziffer, M.E., Snaith, H.J., and Ginger, D.S. (2015). Impact of microstructure on local carrier lifetime in perovskite solar cells. Science *348*, 683–686.

Rehman, W., McMeekin, D.P., Patel, J.B., Milot, R.L., Johnston, M.B., Snaith, H.J., and Herz, L.M. (2017). Photovoltaic mixed-cation lead mixed-halide perovskites: Links between crystallinity, photo-stability and electronic properties. Energy Environ. Sci. *10*, 361–369.

Ren, H., Yu, S., Chao, L., Xia, Y., Sun, Y., Zuo, S., Li, F., Niu, T., Yang, Y., Ju, H., et al. (2020). Efficient and stable ruddlesden–popper perovskite solar cell with tailored interlayer molecular interaction. Nat. Photon. *14*, 154–163.

Rolston, N., Watson, B.L., Bailie, C.D., McGehee, M.D., Bastos, J.P., Gehlhaar, R., Kim, J.-E., Vak, D., Mallajosyula, A.T., Gupta, G., et al. (2016). Mechanical integrity of solution-processed perovskite solar cells. Extreme Mech. Lett. *9*, 353–358.

Ru, P.B., Bi, E.B., Zhang, Y., Wang, Y.B., Kong, W.Y., Sha, Y.M., Tang, W.T., Zhang, P., Wu, Y.Z., Chen, W., et al. (2020). High electron affinity enables fast hole extraction for efficient flexible inverted perovskite solar cells. Adv. Energy Mater. *10*, 1903487.

Saidaminov, M.I., Williams, K., Wei, M., Johnston, A., Quintero-Bermudez, R., Vafaie, M., Pina, J.M., Proppe, A.H., Hou, Y., Walters, G., et al. (2020). Multi-cation perovskites prevent carrier reflection from grain surfaces. Nat. Mater. *19*, 412–418.

Saliba, M. (2019). Polyelemental, multicomponent perovskite semiconductor libraries through combinatorial screening. Adv. Energy Mater. *9*, 1803754.

Saliba, M., Matsui, T., Seo, J.-Y., Domanski, K., Correa-Baena, J.-P., Nazeeruddin, M.K., Zakeeruddin, S.M., Tress, W., Abate, A., Hagfeldt, A., and Grätzel, M. (2016). Cesium-containing triple cation perovskite solar cells: improved stability, reproducibility and high efficiency. Energy Environ. Sci. *9*, 1989–1997.

Samu, G.F., Balog, Á., De Angelis, F., Meggiolaro, D., Kamat, P.V., and Janáky, C. (2019). Electrochemical hole injection selectively expels iodide from mixed halide perovskite films. J. Am. Chem. Soc. *141*, 10812–10820.

Samu, G.F., Janáky, C., and Kamat, P.V. (2017). A victim of halide ion segregation. How light soaking affects solar cell performance of mixed halide lead perovskites. ACS Energy Lett. *2*, 1860–1861.

Sanchez, S., Pfeifer, L., Vlachopoulos, N., and Hagfeldt, A. (2021). Rapid hybrid perovskite film crystallization from solution. Chem. Soc. Rev. *50*, 7108–7131.

Sedighi, R., Tajabadi, F., Shahbazi, S., Gholipour, S., and Taghavinia, N. (2016). Mixed-halide $CH_3NH_3PbI_{3-x}X_x$ (X=Cl, Br, I) perovskites: Vapor-assisted solution deposition and application as solar cell absorbers. ChemPhysChem *17*, 2382–2388.

Shi, J., Li, Y., Wu, J., Wu, H., Luo, Y., Li, D., Jasieniak, J.J., and Meng, Q. (2020). Exciton character and high-performance stimulated emission of hybrid lead bromide perovskite polycrystalline film. Adv. Opt. Mater. *8*, 1902026.

Shirzadi, E., Mahata, A., Roldán Carmona, C., De Angelis, F., Dyson, P.J., and Nazeeruddin, M.K. (2019). Introduction of a bifunctional cation affords perovskite solar cells stable at temperatures exceeding 80 °C. ACS Energy Lett *4*, 2989–2994.

Shockley, W., and Queisser, H.J. (1961). Detailed balance limit of efficiency of p-n junction solar cells. J. Appl. Phys. *32*, 510–519.

Singh, T., and Miyasaka, T. (2018). Stabilizing the efficiency beyond 20% with a mixed cation perovskite solar cell fabricated in ambient air under controlled humidity. Adv. Energy Mater. *8*, 1700677.

Slavney, A.H., Hu, T., Lindenberg, A.M., and Karunadasa, H.I. (2016). A bismuth-halide double perovskite with long carrier recombination lifetime for photovoltaic applications. J. Am. Chem. Soc. *138*, 2138–2141.

Solanki, A., Yadav, P., Turren-Cruz, S.-H., Lim, S.S., Saliba, M., and Sum, T.C. (2019). Cation influence on carrier dynamics in perovskite solar cells. Nano Energy *58*, 604–611.

Son, D.-Y., Kim, S.-G., Seo, J.-Y., Lee, S.-H., Shin, H., Lee, D., and Park, N.-G. (2018). Universal approach toward hysteresis-free perovskite solar cell via defect engineering. J. Am. Chem. Soc. *140*, 1358–1364.

Soon, Y.W., Cho, H., Low, J., Bronstein, H., McCulloch, I., and Durrant, J.R. (2013). Correlating triplet yield, singlet oxygen generation and photochemical stability in polymer/fullerene blend films. Chem. Commun. *49*, 1291–1293.

Steele, J.A., Puech, P., Keshavarz, M., Yang, R., Banerjee, S., Debroye, E., Kim, C.W., Yuan, H., Heo, N.H., Vanacken, J., et al. (2018). Giant electron–phonon coupling and deep conduction band resonance in metal halide double perovskite. ACS Nano. *12*, 8081–8090.

Stoumpos, C.C., Frazer, L., Clark, D.J., Kim, Y.S., Rhim, S.H., Freeman, A.J., Ketterson, J.B., Jang, J.I., and Kanatzidis, M.G. (2015). Hybrid germanium iodide perovskite semiconductors: Active lone pairs, structural distortions, direct and indirect energy gaps, and strong nonlinear optical properties. J. Am. Chem. Soc. *137*, 6804–6819.

Stranks, S.D., Burlakov, V.M., Leijtens, T., Ball, J.M., Goriely, A., and Snaith, H.J. (2014). Recombination kinetics in organic-inorganic perovskites: Excitons, free charge, and subgap states. Phys. Rev. Appl. *2*, 034007.

Stranks, S.D., and Plochocka, P. (2018). The influence of the Rashba effect. Nat. Mater. *17*, 381–382.

Sun, S., Isikgor, F.H., Deng, Z., Wei, F., Kieslich, G., Bristowe, P.D., Ouyang, J., and Cheetham, A.K. (2017). Factors influencing the mechanical properties of formamidinium lead halides and related hybrid perovskites. ChemSusChem *10*, 3740–3745.

Svane, K.L., Forse, A.C., Grey, C.P., Kieslich, G., Cheetham, A.K., Walsh, A., and Butler, K.T.

(2017). How strong is the hydrogen bond in hybrid perovskites? J. Phys. Chem. Lett. *8*, 6154–6159.

Syed, H., Kong, W., Mottamchetty, V., Lee, K.J., Yu, W., Soma, V.R., Yang, J., and Guo, C. (2020). Giant nonlinear optical response in triple cation halide mixed perovskite films. Adv. Opt. Mater. *8*, 1901766.

Tan, W., Bowring, A.R., Meng, A.C., McGehee, M.D., and McIntyre, P.C. (2018). Thermal stability of mixed cation metal halide perovskites in air. ACS Appl. Mater. Interfaces *10*, 5485–5491.

Tennyson, E.M., Roose, B., Garrett, J.L., Gong, C., Munday, J.N., Abate, A., and Leite, M.S. (2019). Cesium-incorporated triple cation perovskites deliver fully reversible and stable nanoscale voltage response. ACS Nano *13*, 1538–1546.

Travis, W., Glover, E.N.K., Bronstein, H., Scanlon, D.O., and Palgrave, R.G. (2016). On the application of the tolerance factor to inorganic and hybrid halide perovskites: A revised system. Chem. Sci. *7*, 4548–4556.

Umebayashi, T., Asai, K., Kondo, T., and Nakao, A. (2003). Electronic structures of lead iodide based low-dimensional crystals. Phys. Rev. B *67*, 155405.

Unger, E.L., Kegelmann, L., Suchan, K., Sörell, D., Korte, L., and Albrecht, S. (2017). Roadmap and roadblocks for the band gap tunability of metal halide perovskites. J. Mater. Chem. A *5*, 11401–11409.

Venugopalan, V., Sorrentino, R., Topolovsek, P., Nava, D., Neutzner, S., Ferrari, G., Petrozza, A., and Caironi, M. (2019). High-detectivity perovskite light detectors printed in air from benign solvents. Chem *5*, 868–880.

Volonakis, G., Filip, M.R., Haghighirad, A.A., Sakai, N., Wenger, B., Snaith, H.J., and Giustino, F. (2016). Lead-free halide double perovskites via heterovalent substitution of noble metals. J. Phys. Chem. Lett. *7*, 1254–1259.

Wang, J.T.-W., Wang, Z., Pathak, S., Zhang, W., deQuilettes, D.W., Wisnivesky-Rocca-Rivarola, F., Huang, J., Nayak, P.K., Patel, J.B., Mohd Yusof, H.A., et al. (2016). Efficient perovskite solar cells by metal ion doping. Energy Environ. Sci. *9*, 2892–2901.

Wang, K., Wu, C., Hou, Y., Yang, D., Ye, T., Yoon, J., Sanghadasa, M., and Priya, S. (2020a). Isothermally crystallized perovskites at room-temperature. Energy Environ. Sci. *13*, 3412–3422.

Wang, S., Wang, A., Deng, X., Xie, L., Xiao, A., Li, C., Xiang, Y., Li, T., Ding, L., and Hao, F. (2020b). Lewis acid/base approach for efficacious defect passivation in perovskite solar cells. J. Mater. Chem. A *8*, 12201–12225.

Wang, L., Zhou, H., Hu, J., Huang, B., Sun, M., Dong, B., Zheng, G., Huang, Y., Chen, Y., Li, L., et al. (2019a). A Eu^{3+}-Eu^{2+} ion redox shuttle imparts operational durability to Pb-I perovskite solar cells. Science *363*, 265–270.

Wang, R., Xue, J., Wang, K.-L., Wang, Z.-K., Luo, Y., Fenning, D., Xu, G., Nuryyeva, S., Huang, T., Zhao, Y., et al. (2019b). Constructive molecular configurations for surface-defect passivation of perovskite photovoltaics. Science *366*, 1509–1513.

Wang, X., Ling, Y., Lian, X., Xin, Y., Dhungana, K.B., Perez-Orive, F., Knox, J., Chen, Z., Zhou, Y., Beery, D., et al. (2019c). Suppressed phase separation of mixed-halide perovskites confined in endotaxial matrices. Nat. Commun. *10*, 695.

Wang, Y.-C., Li, H., Hong, Y.-H., Hong, K.-B., Chen, F.-C., Hsu, C.-H., Lee, R.-K., Conti, C., Kao, T.S., and Lu, T.-C. (2019d). Flexible organometal–halide perovskite lasers for speckle reduction in imaging projection. ACS Nano *13*, 5421–5429.

Wang, J., Li, J., Zhou, Y., Yu, C., Hua, Y., Yu, Y., Li, R., Lin, X., Chen, R., Wu, H., et al. (2021a). Tuning an electrode work function using organometallic complexes in inverted perovskite solar cells. J. Am. Chem. Soc. *143*, 7759–7768.

Wang, P., Chen, B., Li, R., Wang, S., Ren, N., Li, Y., Mazumdar, S., Shi, B., Zhao, Y., and Zhang, X. (2021b). Cobalt chloride hexahydrate assisted in reducing energy loss in perovskite solar cells with record open-circuit voltage of 1.20 V. ACS EnergyLett. 2121–2128.

Wang, S., Pang, S., Chen, D., Zhu, W., Xi, H., and Zhang, C. (2021c). Improving perovskite solar cell performance by compositional engineering via triple-mixed cations. Sol. Energy *220*, 412–417.

Wang, S., Wang, A., Hao, F., and Ding, L. (2021d). Renaissance of tin halide perovskite solar cells. J. Semicond. *42*, 030201.

Wang, S., Hu, J., Wang, A., Cui, Y., Chen, B., Niu, X., and Hao, F. (2022). Facile lattice tensile strain compensation in mixed-cation halide perovskite solar cells. J. Energy Chem. *66*, 422–428.

Wang, Y., Zhang, Y., Zhang, P., and Zhang, W. (2015). High intrinsic carrier mobility and photon absorption in the perovskite $CH_3NH_3PbI_3$. Phys. Chem. Chem. Phys. *17*, 11516–11520.

Wang, Y., Liang, Y., Zhang, Y., Yang, W., Sun, L., and Xu, D. (2018a). Pushing the envelope: Achieving an open-circuit voltage of 1.18 v for unalloyed $mapbi_3$ perovskite solar cells of a planar architecture. Adv. Funct. Mater. *28*, 1801237.

Wang, Z., Lin, Q., Wenger, B., Christoforo, M.G., Lin, Y.-H., Klug, M.T., Johnston, M.B., Herz, L.M., and Snaith, H.J. (2018b). High irradiance performance of metal halide perovskites for concentrator photovoltaics. Nat. Energy *3*, 855–861.

Wu, B., Yuan, H., Xu, Q., Steele, J.A., Giovanni, D., Puech, P., Fu, J., Ng, Y.F., Jamaludin, N.F., Solanki, A., et al. (2019). Indirect tail states formation by thermal-induced polar fluctuations in halide perovskites. Nat. Commun. *10*, 484.

Wei, J., Wang, Q., Huo, J., Gao, F., Gan, Z., Zhao, Q., and Li, H. (2020). Mechanisms and suppression of photoinduced degradation in perovskite solar cells. Adv. Energy Mater. *11*, 2002326.

Wu, S., Li, Z., Zhang, J., Wu, X., Deng, X., Liu, Y., Zhou, J., Zhi, C., Yu, X., Choy, W.C.H., et al. (2021). Low-bandgap organic bulk-heterojunction enabled efficient and flexible perovskite solar cells. Adv. Mater. https://doi.org/10.1002/adma.202105539.

Wu, Z., Li, P., Zhang, Y., and Zheng, Z. (2018). Flexible and stretchable perovskite solar cells: Device design and development methods. Small Methods *2*, 1800031.

Xiao, Z., Yuan, Y., Shao, Y., Wang, Q., Dong, Q., Bi, C., Sharma, P., Gruverman, A., and Huang, J. (2015). Giant switchable photovoltaic effect in organometal trihalide perovskite devices. Nat. Mater. *14*, 193–198.

Xie, L., Song, P., Shen, L., Lu, J., Liu, K., Lin, K., Feng, W., Tian, C., and Wei, Z. (2020). Revealing the compositional effect on the intrinsic long-term stability of perovskite solar cells. J. Mater. Chem. A *8*, 7653–7658.

Xu, J., Boyd, C.C., Yu, Z.J., Palmstrom, A.F., Witter, D.J., Larson, B.W., France, R.M., Werner, J., Harvey, S.P., Wolf, E.J., et al. (2020). Triple-halide wide-band gap perovskites with suppressed phase segregation for efficient tandems. Science *367*, 1097–1104.

Xu, Z., Liu, Z., Li, N., Tang, G., Zheng, G., Zhu, C., Chen, Y., Wang, L., Huang, Y., Li, L., et al. (2019a). A thermodynamically favored crystal orientation in mixed formamidinium/methylammonium perovskite for efficient solar cells. Adv. Mater. *31*, 1900390.

Yang, J., and Kelly, T.L. (2017). Decomposition and cell failure mechanisms in lead halide perovskite solar cells. Inorg. Chem. *56*, 92–101.

Yang, X., Ni, Y., Zhang, Y., Wang, Y., Yang, W., Luo, D., Tu, Y., Gong, Q., Yu, H., and Zhu, R. (2021). Multiple-defect management for efficient perovskite photovoltaics. ACS EnergyLett, 2404–2412.

Ye, T., Wang, K., Ma, S., Wu, C., Hou, Y., Yang, D., Wang, K., and Priya, S. (2021). Strain-relaxed tetragonal $MAPbI_3$ results in efficient mesoporous solar cells. Nano Energy *83*, 105788.

Yin, W.-J., Yang, J.-H., Kang, J., Yan, Y., and Wei, S.-H. (2015). Halide perovskite materials for solar cells: A theoretical review. J. Mater. Chem. A *3*, 8926–8942.

Zhang, C.-X., Shen, T., Guo, D., Tang, L.-M., Yang, K., and Deng, H.-X. (2020a). Reviewing and understanding the stability mechanism of halide perovskite solar cells. InfoMat *2*, 1034–1056.

Zhang, C., Wang, S., Li, X., Yuan, M., Turyanska, L., and Yang, X. (2020b). Core/shell perovskite nanocrystals: Synthesis of highly efficient and environmentally stable $FAPbBr_3/CsPbBr_3$ for led applications. Adv. Funct. Mater. *30*, 1910582.

Zhang, L., and Sit, P.H.L. (2015). Ab initio study of interaction of water, hydroxyl radicals, and hydroxide ions with $CH_3NH_3PbI_3$ and $CH_3NH_3PbBr_3$ surfaces. J. Phys. Chem. C *119*, 22370–22378.

Zhao, H., Li, X., Cai, M., Liu, C., You, Y., Wang, R., Channa, A.I., Lin, F., Huo, D., Xu, G., et al. (2021). Role of copper doping in heavy metal-free InP/ZnSe core/shell quantum dots for highly efficient and stable photoelectrochemical cell. Adv. Energy Mater. *11*, 2101230.

Zhao, J., Deng, Y., Wei, H., Zheng, X., Yu, Z., Shao, Y., Shield, J.E., and Huang, J. (2017). Strained hybrid perovskite thin films and their impact on

the intrinsic stability of perovskite solar cells. Sci. Adv. *3*, eaao5616.

Zheng, G., Zhu, C., Ma, J., Zhang, X., Tang, G., Li, R., Chen, Y., Li, L., Hu, J., Hong, J., et al. (2018). Manipulation of facet orientation in hybrid perovskite polycrystalline films by cation cascade. Nat. Commun. *9*, 2793.

Zheng, X., Chen, B., Dai, J., Fang, Y., Bai, Y., Lin, Y., Wei, H., Zeng, Xiao C., and Huang, J. (2017). Defect passivation in hybrid perovskite solar cells using quaternary ammonium halide anions and cations. Nat. Energy *2*, 17102.

Zheng, X., Hou, Y., Bao, C., Yin, J., Yuan, F., Huang, Z., Song, K., Liu, J., Troughton, J., Gasparini, N., et al. (2020). Managing grains and interfaces via ligand anchoring enables 22.3%-efficiency inverted perovskite solar cells. Nat. Energy *5*, 131–140.

Zheng, X., Wu, C., Jha, S.K., Li, Z., Zhu, K., and Priya, S. (2016). Improved phase stability of formamidinium lead triiodide perovskite by strain relaxation. ACS Energy Lett. *1*, 1014–1020.

Zhu, C., Niu, X., Fu, Y., Li, N., Hu, C., Chen, Y., He, X., Na, G., Liu, P., Zai, H., et al. (2019). Strain engineering in perovskite solar cells and its impacts on carrier dynamics. Nat. Commun. *10*, 815.

Zhu, W., Ma, W., Su, Y., Chen, Z., Chen, X., Ma, Y., Bai, L., Xiao, W., Liu, T., Zhu, H., et al. (2020). Low-dose real-time X-ray imaging with nontoxic double perovskite scintillators. Light Sci. Appl. *9*, 112.

Zu, F.-S., Amsalem, P., Salzmann, I., Wang, R.-B., Ralaiarisoa, M., Kowarik, S., Duhm, S., and Koch, N. (2017). Impact of white light illumination on the electronic and chemical structures of mixed halide and single crystal perovskites. Adv. Opt. Mater. *5*, 1700139.